Simultaneous extraction of the elastic-plastic properties of a thin film and its substrate from an identifiability-based design of depth-sensing nanoindentation testing

Vincent Fauvel [1,2], Yves Gaillard [1], Raphaël Guillemet [2], Patrick Garabédian [2],
Fabrice Richard [1]

[1] Université Bourgogne Franche-Comté, Institut FEMTO-ST, CNRS/UFC/ENSMM/UTBM,
Département de Mécanique Appliquée, 24 rue de l'Epitaphe, 25000 Besançon, France

[2] THALES Research & Technology, 1 avenue Augustin Fresnel, 91120 Palaiseau, France

Abstract

This work presents an approach to simultaneously identify reliable elasto-plastic properties of a 100 nm amorphous alumina film and plastic properties of its silicon substrate by the Finite Element Model Updating (FEMU) method, using exclusively nanoindentation $P - h$ curves. A 2D axisymmetric finite element model simulates the nanoindentation tests, and the Young's modulus E, the initial yield stress σ_y and the hardening modulus H_p of the thin film, as well as the yield stress of silicon σ_{ys} are the parameters to identify. This work relies on a numerical design of experiments carried prior to the identification process. It uses the sensitivity of the nanoindentation force to a variation of the parameters to define an identifiability indicator (I-index) based on the conditioning of the inverse problem. It reflects the stability of the potential solution of the inverse problem. I-index minimisation below a certain value allows to ensure a reliable identification by designing the best combination of experiments in terms of relevant information. I-index analyses values demonstrate that combining Berkovich and cube corner nanoindentation tests at two different indentation depths brings sufficient information to well-conditioned the inverse problem. Indeed, the increased penetration and the varied indenter tip shape induce differentiating factors which activates the substrate effect, or anvil effect, and allow the dissociation of the thin film plasticity from that of the substrate, and thus its identification. The identification procedure of the four parameters carried out with the designed dual nanoindentation test from several starting points reveals that the FEMU method converged to a unique solution. Lastly, the identified parameters are validated by confronting experimental and numerical (i) $P - h$ curves of a Berkovich test on a bulk silicon sample and (ii) residual topographies using a 3D FEM of a Berkovich test on the composite system thin film – substrate.

Keywords: Nanoindentation, Identifiability analysis, Inverse method, Parametric identification, Thin film, Anvil effect

1. Introduction

Instrumented indentation, also named nanoindentation, is a popular technique for the study of materials mechanical properties at the submicrometric scale. As its name suggests, instrumented indentation allows monitoring the load and the penetration of a tip with known geometry, driven by a load depth step up to a maximum value P_{max} (or h_{max}), followed by the withdrawal of the indenter to zero. This technique is one of a few to allow testing the hardness of thin films, for which the range of thickness can go from around 50 nm to several microns, as it requires very small indentations. To that end, depth-sensing instruments are needed to provide the necessary resolution and reproducibility to record the penetration of the indenter into the material for hardness measurements.

The material behaviour towards indentation may be fully elastic, elastic and plastic, or even fully plastic, and the combination of these responses is subtly reflected by the recorded nanoindentation curve. Therefore, a suitable model is required to understand and calculate the elastic and plastic contributions to the displacement. One of the most widespread method in this sense has been proposed by Oliver and Pharr (Oliver & Pharr, 1992, 2004). This model is based on analytical calculations carried out by Sneddon (Harding & Sneddon, 1945; Sneddon, 1948, 1965), which states the common framework for axisymmetric indentation without friction.

The accuracy of Oliver and Pharr analysis for the estimation of indentation hardness and modulus highly depends on the measurement of the projected contact area at maximum load A_c. In practice, measuring accurately this area with depth-sensing instruments is challenging since plastic pile-up or elastic sink-in can occur and affect the size of the true contact area (Field & Swain, 1993; Le Bourhis, 2008). The eventuality of pile-up is hardly taken into account in this method. Thus, the projected contact area is likely to be underestimated leading to an overestimated indentation modulus or hardness.

For purposes of extracting the intrinsic mechanical properties of thin films, dissociate the influence of the underlying substrate on the measured mechanical properties is needed. Indeed, the resulted indentation modulus and hardness from the Oliver and Pharr method in this case correspond to the combined/composite system substrate – coating, where the substrate effect on the estimated properties indentation is non-negligible, in particular with submicrometric films.

Analytical models can be used to extract intrinsic elastic modulus of thin films. In 1992, Gao *et al.* proposed a model based on the analysis of the elastic contact between a flat punch and a film – substrate system to determine the shear modulus of the film (Gao et al., 1992). Each material compliance is function of the shear modulus of the film and the substrate and their Poisson coefficients through two weight functions, which depends on e/a ratio, where e is the film thickness and a the contact radius of the indenter tip. Another model is proposed by Bec *et al.* in 1996, based on the indentation of a rigid cylindrical flat punch of an homogeneous thin film deposited on a substrate (Bec et al., 1996, 2006). This composite system is modelized by two springs connected in series, whose stiffness depends on the contact radius of the indenter tip a, the film thickness e and the reduced modulus of each material.

These methods use the Continuous Stiffness Measurements (CSM) technique, however several limitations exists in the application of such models for the extraction of elastic modulus of ultra-thin film (from around 50 nm to 200 nm). At low depths, measurements uncertainties can be significant, and the effect of surface rugosity is non-negligible. What's more, Pharr *et al.* have shown that displacement oscillations used in CSM nanoindentation can generate significant dispersions on the measured elastic modulus (Pharr et al., 2009). Plastic pile-up around the imprint is also hardly taken into account in these methods and, as the CSM technique uses the Oliver and Pharr model, it affects the measurement of the projected contact area, and thus elastic modulus calculations. Finally, these methods don't allow to extract plastic properties, like a yield stress and a hardening modulus. Given these difficulties, estimating mechanical properties of the coating, strictly, from experimental measurements is challenging, and can be helped with finite element modelling simulations.

Over the past twenty years, computation means have allowed the simulation of experiments involving more and more complex material behaviours. The numerical approach allows to achieve plenty of simulations of indentation tests in a short amount of time and brings an ease for tailoring experiments by integrating material subtleties like sample anisotropy or viscosity (L. Cheng et al., 2000; Y.-T. Cheng & Cheng, 2004; Daphalapurkar et al., 2009; Huang et al., 2008; Peng et al., 2013), but also indenter tip blunting (Bei et al., 2005; Keryvin et al., 2017; Lu & Bogy, 1995; Shih et al., 1991; Torres-Torres et al., 2010; T. H. Wang et al., 2007; Youn & Kang, 2005). This approach also offers the integration of materials elasto-plastic behaviours for both substrate and coating, and thus allow the identification of the intrinsic elasto-plastic properties of thin films (Cai & Bangert, 1995; Lichinchi et al., 1998).

This convenience motivates the predictive search for the most reliable experiment to identify elastic and plastic behaviour of thin films. In that sense, the use of the inverse analysis is suitable to reliably estimate elasto-plastic properties of thin films by modelling nanoindentation experiments (Zhao et al., 2006, 2007; Pac et al., 2014; Qasmi et al., 2006).

The inverse analysis relies on the knowledge of the response of the modelized system to deduct parameters which describe the mechanical behaviour of this system. The inverse analysis of a nanoindentation numerical model covers several methods, like the Finite Element Model Updating (FEMU) method (Kavanagh, 1972; Kavanagh & Clough, 1971), the dimensionless functions method (Y.-T. Cheng & Cheng, 1998a, 1998b), or the neural network approach (Yagawa & Okuda, 1996). Whatever the method used, the main purpose is identical: identify the parameters of a material behaviour law.

With that said, numerous works (Alkorta et al., 2005; Capehart & Cheng, 2003; Casals & Alcalá, 2005; Y.-T. Cheng & Cheng, 1999; Tho et al., 2004) have shown that multiple combinations of elasto-plastic parameters describing different materials mechanical behaviours may lead to the same indentation $P - h$ curve. The solution of the inverse problem is thus non-unique, hence the stress-strain relationship describing the material mechanical behaviour may not be uniquely determined by using a single nanoindentation test. It suggests that additional information is required. To that end, the combination of multiple nanoindentation tests performed with differentiating factors could enrich the inverse problem. It may be different indentation depths, different indenter tip geometries (Bucaille et al., 2003; Cao & Lu, 2004; Chollacoop et al., 2003; DiCarlo et al., 2003; Futakawa et al., 2001; Heinrich et al., 2009; Lan & Venkatesh, 2007; Le, 2008, 2009; Luo & Lin, 2007; Phadikar et al., 2013; Swaddiwudhipong et al., 2005; L. Wang et al., 2005; Yan et al., 2007, 2007), or by adding the topography of the residual imprint (Bocciarelli et al., 2005, 2008; Bocciarelli & Bolzon, 2009; Bolzon et al., 2004, 2009, 2011; Ma et al., 2012; Renner, 2016; Renner et al., 2020).

This work investigates the possibility to reliably extract three elasto-plastic parameters of an alumina thin film as well as the yield stress of the silicon substrate using $P - h$ curves from nanoindentation experiments on a thin film/subtrate system. The optimal design of experiments, (well-posedness of the inverse problem), is investigated with an identifiability analysis performed prior to the identification process. This approach is also known as *a priori* identifiability or structural identifiability, and depends only on the model and simulated data (Anstett-Collin et al., 2020; Walter & Pronzato, 1997). In this work, *a priori* identifiability is mainly carried out through an identifiability indicator (I-index), which reflects the stability of the inverse problem solution and allows to quantify the information richness contained in the experiments (Pac et al., 2014; Richard et al., 2013). In other terms, this indicator acts as a guide for a good conditioning of the inverse problem. In particular, this work studies the impact of the maximum indentation depth and the indenter tip geometry on I-index calculations. The designed experiment is then realised experimentally and implemented into the identification process for an optimum estimation of material elasto-plastic parameters. Thereafter a practical identifiability, which differs from the *a priori* identifiability as it is based on real experimental measurements, is performed *a posteriori* of the identification process to judge the fit quality of the model to experimental data. Lastly, a validation of the set of identified parameters is realised by confronting: (i) the numerical and experimental $P - h$ curves of a nanoindentation test on the bulk silicon substrate and (ii) the numerical and experimental topography of the imprint of a nanoindentation test on the composite alumina thin film - silicon substrate sample.

2. Materials and methods

2.1. Experimental details

2.1.1. Alumina thin film deposition

Amorphous alumina (Al_2O_3) thin film has been deposited on an oriented (100) silicon substrate at 200°C by plasma enhanced atomic layer deposition with trimethylaluminium (TMA) precursor and O_2 gas, with a targeted thickness of 100 nm. This thickness has been confirmed with an UVISEL Ellipsometer. The surface morphology characterisation of Al_2O_3 film has been performed by Atomic Force Microscopy and shows excellent conformity and large-area uniformity with a root mean square rugosity of about 0.5 nm.

2.1.2. Nanoindentation experiments

Nanoindentation experiments have been performed at room temperature and humidity using an Anton Paar nanoindenter with Ultra Nano Hardness Tester (UNHT) head with either Berkovich or cube corner indenter tip. All nanoindentation experiments have been carried out in displacement-controlled mode with a triangular loading and unloading phase, with equal time for the 2 phases.

2.2. Material constitutive law of thin film and substrate

The mechanical behaviour of each material which constitutes composite system thin film - substrate can be modelled by a bilinear elasto-plastic law. The total strain tensor ε_{ij} is decomposed between elastic and plastic contributions, respectively ε_{ij}^{e} and ε_{ij}^{p}, as:

$$\varepsilon_{ij} = \varepsilon_{ij}^{e} + \varepsilon_{ij}^{p}. \tag{2.1}$$

The elastic contribution is driven by the Young's modulus E and the Poisson's coefficient ν, the two intrinsic elastic parameters linking stress and strain by Hooke's law, defined in the case of isotropic linear elastic materials by:

$$\sigma_{ij} = \frac{E}{1+\nu}\left(\varepsilon_{ij}^{e} + \frac{\nu}{1-2\nu}\varepsilon_{kk}^{e}\delta_{ij}\right). \tag{2.2}$$

σ_{ij} is the Cauchy stress tensor, ε_{kk}^{e} is the trace of the strain tensor ε_{ij}^{e} and δ_{ij} is the Kronecker delta.

The plastic contribution is driven by the initial tensile yield stress σ_y of the material and its isotropic hardening modulus H_p. It is related to the von Mises yield stress criterion, which defines the stress threshold from which the material plastically deforms.

In the case of a uniaxial tensile test, these assumptions on the elastic and plastic behaviour can be written as:

$$\sigma = E\varepsilon \qquad \text{for} \quad \sigma < \sigma_y \tag{2.3}$$

$$\sigma = \frac{EH_p}{E + H_p}\varepsilon \quad \text{for} \quad \sigma \geq \sigma_y. \tag{2.4}$$

where σ is the Cauchy tensile stress and ε is the logarithmic tensile strain.

The alumina thin film is assumed elasto-plastic with linear isotropic plastic hardening and described by its elastic (E, ν) and plastic parameters (σ_y, H_p). The Poisson's ratio of the thin film is assumed and fixed at 0.3 and $E \equiv \theta_1$, $\sigma_y \equiv \theta_2$ and $H_p \equiv \theta_3$ are unknown and identified using the FEMU method described in section 2.4, based on the numerical design of experiment described in section 2.4.

As for the silicon substrate, it is supposed isotropic elastic perfectly plastic. The Young's modulus E and Poisson's ratio of silicon are isotropic equivalent values fixed at 173 GPa and 0.21 respectively (Hall, 1967; Hill, 1952). Note that the Young's modulus value of silicon was experimentally validated on a bulk sample from a Berkovich nanoindentation test using the Oliver&Pharr method (Oliver & Pharr, 1992) and is in accordance with the value derived from literature (Pac et al., 2014). The silicon yield stress σ_{ys} is first fixed at 5 GPa, with a value derived from literature (L. Zhang & Mahdi, 1996). Thereafter, this parameter $\sigma_{ys} \equiv \theta_4$ is released and identified on top of the three elasto-plastic parameters E, σ_y and H_p of the thin film. Table 1 summarises values of each known and unknown parameter used in the composite system thin film - substrate.

2.3. Finite element models of the nanoindentation experiment

The nanoindentation test is modelled using ANSYS Mechanical APDL software. In this work a 2D axisymmetric finite element model (FEM) is used for the identifiability analysis and the identification process for the sake of computing time reduction, and a 3D FEM is used afterward for the validation of the estimated parameters with the topography of the imprint.

2.3.1. 2D axisymmetric FEM

The 2D-axissymetric model geometry and mesh is presented in Figure 1.

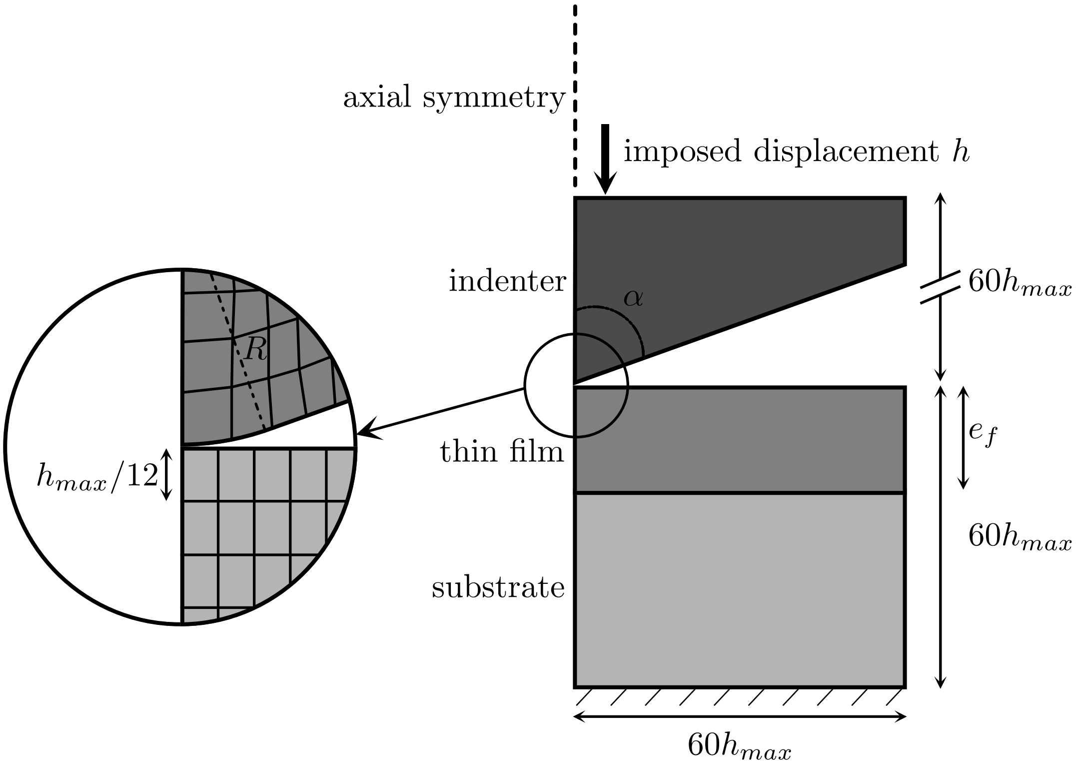

Figure 1: Schematic illustration of the 2D axisymmetric model geometry and mesh used for nanoindentation simulations, with R the indenter radius curvature, α the indenter equivalent half angle, e_f the thin film thickness and h_{max} the maximum indentation depth.

The diamond tip is considered isotropic elastic, described by its elastic parameters (E, ν) fixed at 1141 GPa (Young's modulus) and 0,07 (Poisson's ratio) respectively and stem from the literature (Oliver & Pharr, 1992). The indenter is geometrically defined by an equivalent conical half angle and a tip curvature radius, and its size is set to be sixty times greater than the maximum nanoindentation depth ($60h_{max}$). In this work a cube corner and a Berkovich tip have been used, corresponding respectively to a 42.3° and 70.3° equivalent half angle with a 35 nm and 116 nm tip radius curvature respectively, reported in Table 1. The mesh of the indenter, including its tip, is composed of a 4-node rectangular element mesh zone with 2x2 integration points. The mesh is refined close to the indenter tip and becomes gradually coarser as the distance from the tip increases.

The material constitutive law of thin film and substrate is detailed in section 2.2, and their associated parameters are summarised in Table 1. The size of the specimen modelling the film and the substrate is chosen to be sixty times greater than the maximum nanoindentation depth h_{max}, to limit the effect of boundary conditions. To study the effect of its size on $P - h$ observables, several factors d (dh_{max}), from 40 to 70, have been tested on Berkovich and cube corner tests. The average absolute value of the relative error between the force P_d (from simulations with factor d) and the reference force $P_{ref} = P_{80}$ (from simulation with factor $d = 80$) at any displacement point h_k, normalized by the maximum force of the reference simulation, written as:

$$\Delta P_d = \frac{\overline{|P_d - P_{80}|}}{\max(P_{80})} = \frac{1}{N\max(P_{80})}\sum_{k=1}^{N}|P_d(h_k) - P_{80}(h_k)|, \tag{2.5}$$

have been calculated and shows no influence on the force values, with ΔP_d below 0.5% for each simulation.

The mesh of the sample is composed of a refined 4-node rectangular element mesh zone with 2x2 integration points close to the contact of the indenter, covering the thin film thickness $e_f = 100$ nm and a length of two times the film thickness over the substrate, surrounded by a gradually coarser 6-node triangular element mesh zone with 3 integration points as the distance from the indented area increases. The size of the element just below the indenter is $h_{max}/12$, size for which the convergence of the finite element model is achieved whatever the tip used (Berkovich or cube corner).

The mesh is composed of around 15000 elements. The mesh is blocked at the bottom and a displacement h is imposed to the indenter head. The contact between the indenter and the sample is modelled with a Lagrange multiplier algorithm on contact normal and a penalty on tangent contact defined by a friction coefficient μ of 0.1. Its effect on the nanoindentation force has been shown to be negligible in the case of Berkovich tests by Bucaille *et al.* through 2D axisymmetric simulations on an aluminium allow described by an elasto-plastic power law (Bucaille et al., 2003). For a cube corner test, its effect on the nanoindentation force has been studied using the same analysis on which Equation (2.7) is based, with μ values from 0.1 to 0.5, and considering a reference force from simulation with $\mu = 0$. This study shows that its influence is negligible, with an average absolute value of the relative error below 4% regardless of the value of μ.

	Indenter (diamond)		Thin film (Al_2O_3)	Substrate (Si)
	Berkovich	Cube corner		
Dimensional properties	Semi-infinite blunt cone Tip radius $R = 116$ nm	Semi-infinite blunt cone Tip radius $R = 35$ nm	Thickness $e_f = 100$ nm	Semi-infinite plane
Behaviour	Elastic		Elasto-plastic with linear isotropic hardening	Elastic perfectly plastic
ν	0.07		0.3	0.21
E	1141 GPa		θ_1 unknow	173 GPa
σ_y	∞		θ_2 unknow	5 GPa in §3.1 and §3.2 θ_4 unknow in §3.3
H_p	-		θ_3 unknow	0

Table 1: Parameters used for the diamond indenter, the silicon substrate and the alumina thin film in the FEM of the nanoindentation test.

2.3.2. 3D FEM

In this 3D FEM, the modelled diamond indenter tip is a sixth of a Berkovich tip with an inner angle of 65.3°. The size of the 3D model is thus reduced to a sixth of its real volume, which allows a significant reduction of the number of elements and a decrease of the computation time.

The size of the modelled sample is chosen to be sixty times greater than the maximum nanoindentation depth h_{max}, to limit the effect of boundary conditions. The mesh of the sample is composed of a refined 10-node tetrahedral element mesh zone with 4 integration points close to the contact of the indenter, covering a length ten times greater than the maximum nanoindentation depth h_{max}, which becomes gradually coarser as the distance from the indented area increases. The size of the element just below the Berkovich tip has been determined from a convergence study on two observables: (i) $P - h$ curve and (ii) imprint topography for several element sizes, defined by h_{max}/m, with h_{max} the maximum indentation depth and m a mesh factor, from 3.5 to 10. The same analysis on which Equation (2.5) is based, have been used for $P - h$ observables, considering a reference force from simulation with $m = 12$. For imprint topography observables, the average absolute value of the relative error between the topography value Z_m (from simulations with mesh factor m) and the reference topography $Z_{ref} = Z_{12}$, is calculated at any point in the XY_k plane and normalized by the maximum topography value (*i.e.* maximum height) of the reference simulation, written as:

$$\Delta Z_m = \frac{|\overline{Z_m - Z_{12}}|}{\max(Z_{12})} = \frac{1}{N \max(Z_{12})} \sum_{k=1}^{N} |Z_m(XY_k) - Z_{12}(XY_k)|. \tag{2.6}$$

The average absolute value of the relative error on the force and on the topography value stays respectively below 0.05% and 0.5% regardless of the value of m. For both observables, meshes for which $m > 4$ implies substantial calculation times, close to 10 hours for $m = 6$, jumping to 50 hours for $m = 8$. In that respect, a mesh factor of 4 has been chosen, which is a good compromise between calculation time, about 1h30, and mesh fineness.

The mesh is composed of around 26000 elements and is clamped at the bottom. The contact between the indenter and the sample is modelled with a Lagrange multiplier algorithm on contact normal and a penalty on tangent contact defined by a friction coefficient of 0.1.

2.4. Identification process based on the FEMU method

The Finite Element Model Updating method (FEMU) allow the identification of the material constitutive law with its associated elasto-plastic parameters. From a starting point θ^0, this procedure allows, by the coupling of the FEM and an iterative optimisation algorithm, the estimation of one or more parameters $\hat{\theta}$ by minimising the difference between the force resulting from FE simulation P and the experimental data P^{exp}. Here the inverse problem is a minimisation problem in a least square sense, for which the formulation of a cost function ω, or objective function, allows to quantify the distance between the numerical results and the experimental data. Therefore, the inverse problem can be written as:

$$\hat{\theta} = \operatorname{argmin} \omega[P(h;\theta), P^{exp}(h)], \tag{2.7}$$

where h is the displacement and ω is the cost function to minimise (Qasmi et al., 2004) defined as:

$$\omega(\theta) = \frac{1}{2T} \sum_{k=1}^{T} \left(\frac{P_k(\theta) - P_k^{exp}}{P_{max}^{exp}} \right)^2, \tag{2.8}$$

for one displacement controlled nanoindentation test. T is the number of data points, thus the number of measured numerical P_k and experimental P_k^{exp} force values. P_{max}^{exp} is the maximum experimental force. The number of data points T is equal to 800 with the same number of data points for the loading and unloading part, thus equal to 400. The normalisation of the sum term by P_{max}^{exp} allows to consider dimensionless quantities and an absolute uncertainty on P_k. A variant of the Levenberg-Marquardt algorithm (Levenberg, 1944; Marquardt, 1963), is used to minimise ω with high convergence speed while constraining parameters to positive-only values. This optimization algorithm is implemented in MIC2M (http://mic2m.univ-fcomte.fr/) software (Richard, 1999, 2017).

In an inverse analysis, it must be ensured that the inverse problem is well-posed. The formulation of a well-posed inverse problem must verify that (i) a quasi-solution exist, which ensures an acceptable gap between the numerical results and the experimental data, (ii) this solution is unique, and (iii) this solution is stable *i.e.* that a small perturbation of the $P - h$ observables does not induce a high variation of the parameters (Hadamard, 1902, 1932).

If the existence of a solution can easily be verified *a posteriori* of the updating process by judging the fit quality of the experimental and simulated $P - h$ curves with the cost function value ω, the verification of the unicity and stability however is a major difficulty. Indeed, this implies lots of FEMU procedures with the test of numerous starting points (unicity) and perturbations of $P - h$ observables including different hypothesis on the experimental errors (stability), causing a multiplication of simulations very time-consuming.

With that said, the stability of the potential solutions can be verified prior to the updating process by performing an identifiability analysis. This approach is also known as *a priori* identifiability or structural identifiability, and depends only on the model and simulated data (Anstett-Collin et al., 2020; Walter & Pronzato, 1997). In this work the *a priori* identifiability is mainly carried out through an identifiability indicator called I-index (Pac et al., 2014; Richard et al., 2013) which thus reflects the local stability of the solution and helps design the experiments for a good conditioning of the inverse problem. This identifiability indicator is presented in the following section.

However it is worth noting that, although the non-unicity of the solution has been shown to be a consequence of its instability (Phadikar et al., 2013), the verification of its stability through an *a priori* identifiability is still not sufficient to assess the unicity of the solution. To that end, it is still appropriate to widely explore the space of parameters definition domain *a posteriori* of the updating process by selecting several sets of parameters far from each other to ensure that each of these starting points converge to the same result.

2.5. Numerical design of experiment based on identifiability index

The identifiability index proposed by Richard *et al.* (Richard et al., 2013) is based on the conditioning of the inverse problem, which is the sensitivity of the inverse problem solution, *i.e.* the set of parameters θ,to a perturbation of the nanoindentation force P. Calculated *a priori* of the updating process from simulated experiments with hypothetical material parameters, this index reflects the local stability of the solution. In particular I-index not only integrates and quantifies a lack of sensitivities of the indentation force to parameters, but also the information about an eventual multicollinearity between these sensitivity vectors, which may generate an instable solution of the inverse problem, its non-uniqueness and therefore multiple solutions using the FEMU method.

In that respect, I-index ensures that experiments used in the updating process contains sufficient information to reliably estimate elasto-plastic parameters of the thin film. I-index can be defined with logarithmic notation (Pac et al., 2014) as:

$$I = \log_{10}\left(\frac{\lambda_{max}}{\lambda_{min}}\right). \tag{2.9}$$

where λ_{max} and λ_{min} are the extremal eigenvalue of the quasi-hessian matrix $\bar{H}$ close to the cost function minimum, defined as:

$$\bar{H}_{ij} = \sum_{k=1}^{T} \frac{\partial \bar{P}_k}{\partial \bar{\theta}_i} \frac{\partial \bar{P}_k}{\partial \bar{\theta}_j}, \tag{2.10}$$

where $\frac{\partial \bar{P}_k}{\partial \bar{\theta}_i}$ is the dimensionless sensitivity of the observed force P to the parameter θ_i for the acquisition point k:

$$\frac{\partial \bar{P}_k}{\partial \bar{\theta}_i} = \frac{P_k(\theta_i + \epsilon\theta_i, h) - P_k(\theta_i, h)}{P_{max}\epsilon\sqrt{T}}. \tag{2.11}$$

$P(h)$ is the force response at depth h and $\epsilon = 0.5\%$ is the disturbance value for the numerical derivation. Note that P and θ_i are rendered dimensionless by respectively dividing them by the maximum numerical indentation load P_{max} and ϵ which is designate by the overline notation. Hence it is possible with this formulation to consider responses of different nature (nanoindentation $P - h$ curves or topographies). Nevertheless, the dimensionless matrix $\bar{H}$ as written here is only valid for one nanoindentation loading-unloading curve. The normalisation by $\sqrt{T}$ provides a consistent definition of the sensitivity variation with the cost function defined in equation (2.8) and ensures the independence of the I-index from the number of acquisition points.

The norm of the dimensionless sensitivity variation is used in this work to evaluate the degree of sensitivity of the force P to each parameter θ_i, defined as:

$$\left\|\frac{\partial \bar{P}}{\partial \bar{\theta}_i}\right\|_2 = \sqrt{\sum_{k=1}^{T}\left(\frac{\partial \bar{P}_k}{\partial \bar{\theta}_i}\right)^2} \tag{2.12}$$

In this work the data point k is normalised by the total data points T. Thus, this fraction describes the evolution of the nanoindentation test from 0 to 1, where 0 is the beginning of the loading phase, 0.5 is the beginning of the unloading phase and 1 is the end of the experiment.

This I-index can be interpreted as an indicator of the cost function convexity. This function can be graphically represented, in the case of two parameters θ_1 and θ_2, in a two-dimensional space of dimensionless parametric uncertainties $(\Delta\bar{\theta}_1, \Delta\bar{\theta}_2)$. In the principal base of the matrix $\bar{H}$, this function is an ellipsis of equation:

$$\lambda_1 x_1^2 + \lambda_2 x_2^2 = \omega, \tag{2.13}$$

whose semi-major axis a and semi-minor axis length b directly depend on the eigenvalues $\lambda_1 = \lambda_{min}$ and $\lambda_2 = \lambda_{max}$ of the matrix $\bar{H}$ in equation (2.10):

$$\begin{cases} a = \sqrt{\dfrac{\omega}{\lambda_1}} \\ b = \sqrt{\dfrac{\omega}{\lambda_2}} \end{cases} \tag{2.14}$$

This ellipsis, represented in Figure 2 for different value of I-index, graphically delimitates the region of parameter possibilities.

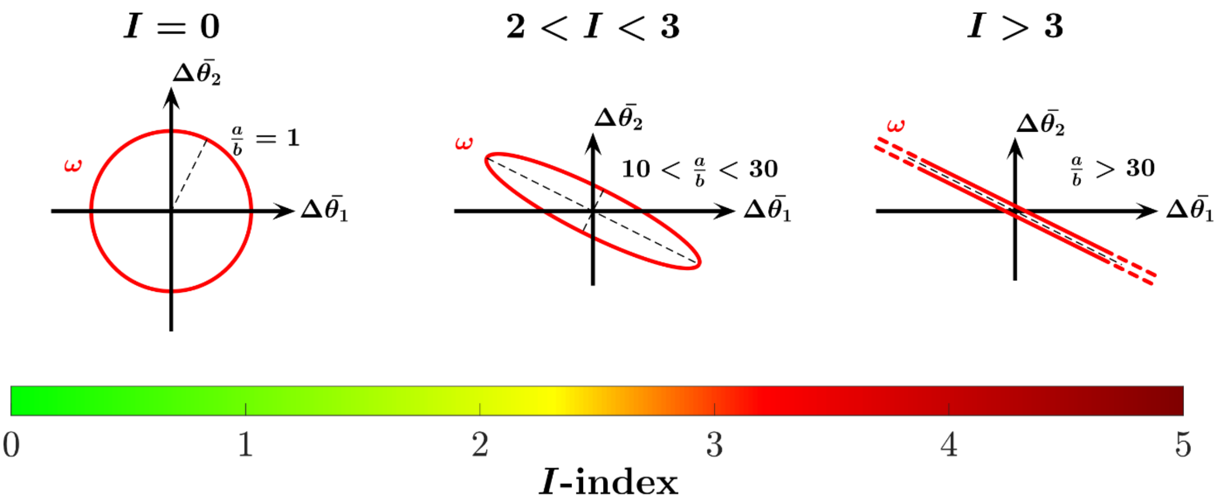

Figure 2: Schematic shapes of the cost function ω in a 2D space of parametric uncertainties for different values of I-index.

Note that for the sake of comprehension Figure 2 is a graphical representation in the case of two parameters, however I-index can also be calculated for more than two parameters. From equation (2.9) and (2.14) the I-index can be rewritten as:

$$I = 2\log_{10}\left(\frac{a}{b}\right) \tag{2.15}$$

Hence the value of I is related to the ratio of the two ellipsis axes. Therefore, the more a and b are different, the larger the value of I is, and the more the cost function used in the FEMU method will be stretched in one direction, sign of a solution valley with high uncertainties when $I > 3$. A local numerical optimisation algorithm, such as the Levenberg-Marquardt algorithm, will not ensure the non-existence of local minimas of the cost function, and that each optimization path may reach the same result.

Richard et al. (Richard et al., 2013) defined a good conditioning of the inverse problem for $I < 2$. That being said, it is important to precise that this criterion is only indicative. The I-index is first and foremost a conditioning number intended to quantitatively compare the richness of information contained in various observation fields with a guiding principle of the lower its value, the better the inverse problem will be conditioned. It works with all methods which require gradient evaluation of a cost function (*e.g.* Gauss-Newton, Levenberg-Marquardt) and based on quasi-hessian matrix $\overline{H}$ (Equation (2.10)).

3. Results and discussion

The interests of the *a priori* identifiability analysis to guide the design of experiments to reliably identify material elasto-plastic parameters have been highlighted in the previous section. Indeed, instability problems induced by the lack of sensitivity of the force response and the eventual sensitivity vectors multicollinearity of the parameters have been raised, and these aspects are reflected by the I-index.

In the following sections, the influence of the maximal indentation depth and the indenter tip geometry on the identifiability of the elasto-plastic parameters of the thin film E, σ_y and H_p is determined to design the experiments to consider for the subsequent identification process. Then, from an *a posteriori* I-index calculation, the inclusion of the substrate yield stress in the identification process on top of the three elasto-plastic parameters of the film is considered and supported by a further *a priori* identifiability analysis. Lastly, a validation of the set of identified parameters is achieved by confronting (i) the numerical and experimental $P - h$ curves of a nanoindentation test on the silicon substrate and (ii) the numerical topography obtained with the 3D FEM and the experimental topography of the imprint of a nanoindentation test on the alumina thin film – silicon sample.

3.1. Numerical design of experiments based on *a priori* identifiability

This section concerns the numerical design of experiments for the identification of the three thin film elasto-plastic parameters $\theta_1 \equiv E$, $\theta_2 \equiv \sigma_y$ and $\theta_3 \equiv H_p$, with $\theta_4 \equiv \sigma_{ys}$ fixed at 5 GPa (L. Zhang & Mahdi, 1996). Sensitivity and I-index calculations are initiated from a starting point $\theta^{01}(E = 200 \text{ GPa}, \sigma_y = 1 \text{ GPa}, H_p = 5 \text{ GPa})$, which defines a postulated potential solution of the inverse problem.

3.1.1. Influence of the maximal indentation depth

The identifiability analysis is first applied to finite element simulations of a single nanoindentation test for 25, 50, and 100 nm maximum depths, using Berkovich tip.

Figure 3 shows the evolution of the force sensitivity with respect to k/T ratio (0 to 0.5 is the loading phase and 0.5 to 1 is the unloading phase) and sensitivity norm for the perturbation ϵ of each initial value of E, σ_y and H_p in θ^{01}, as well as the collinearity between sensitivity vectors of σ_y and H_p for the three indentation depths.

The effect of numerical perturbations on the $P - h$ curve and on I-index values has been studied through polynomial interpolation. A sixth-degree polynomial interpolation induces an error inferior to 1% on the $P - h$ curve and an insignificant impact on I-index values considering the roundness to the nearest tenth.

The norm of the sensitivity for E, σ_y and H_p in Figure 3c reveals that the nanoindentation force is sensitive to all variables, and gradually becomes less sensitive to E and σ_y with the indentation depth, while the influence of H_p remains constant. The yield stress of the thin film σ_y has the strongest influence on the force response for the 25 and 50 nm experiments and has a similar influence with H_p for $h_{max} = 100$ nm. Figure 3a reveals that the sensitivity vectors of the three variables during the loading phase are collinear, suggesting a strong correlation of their influence on the force response. However, the influence on the force of E becomes opposite once the unloading phase starts. It suggests that the unloading segment is more relevant to dissociate the effects of each parameter on the force response, and thus to reliably identify them. However, regardless of the maximum indentation depth, the similar influence of σ_y and H_p on the force response, highlighting by the collinearity between their sensitivity vectors in Figure 3b during the two phases, makes their identification impossible, using only a single nanoindentation curve.

The values of the I-index is shown in Figure 4, for the three h_{max} tested. The values of $I(E,\sigma_y,H_p)$ after the loading and unloading phases converge to 3.0, 2.7 and 2.6 respectively for the 25, 50 and 100 nm experiments. It reveals that the identification of E, σ_y and H_p using a single nanoindentation test, regardless of the indentation depth, is impossible. Although the best value of I-index obtained $h_{max} = 100$ nm is not sufficiently low to lead to a well-posed problem, its evolution suggests that the problem well-posedness has been improved, by increasing the maximum indentation depth. What's more, Figure 4 reveals that the two phases are complementary and bring stability to the I-index as it decreases from the sole loading or unloading phase.

What's more, the calculation of $I(\sigma_y, H_p)$, equal to 2.5, 2.1 and 2 for the 25, 50 and 100 nm experiments respectively, reveals that the deeper the indentation is, the more the problem well-posedness is improved to the point where it should be possible to identify the two plastic parameters, knowing the two elastic parameters (E,ν) of the film and the mechanical behaviour of the substrate.

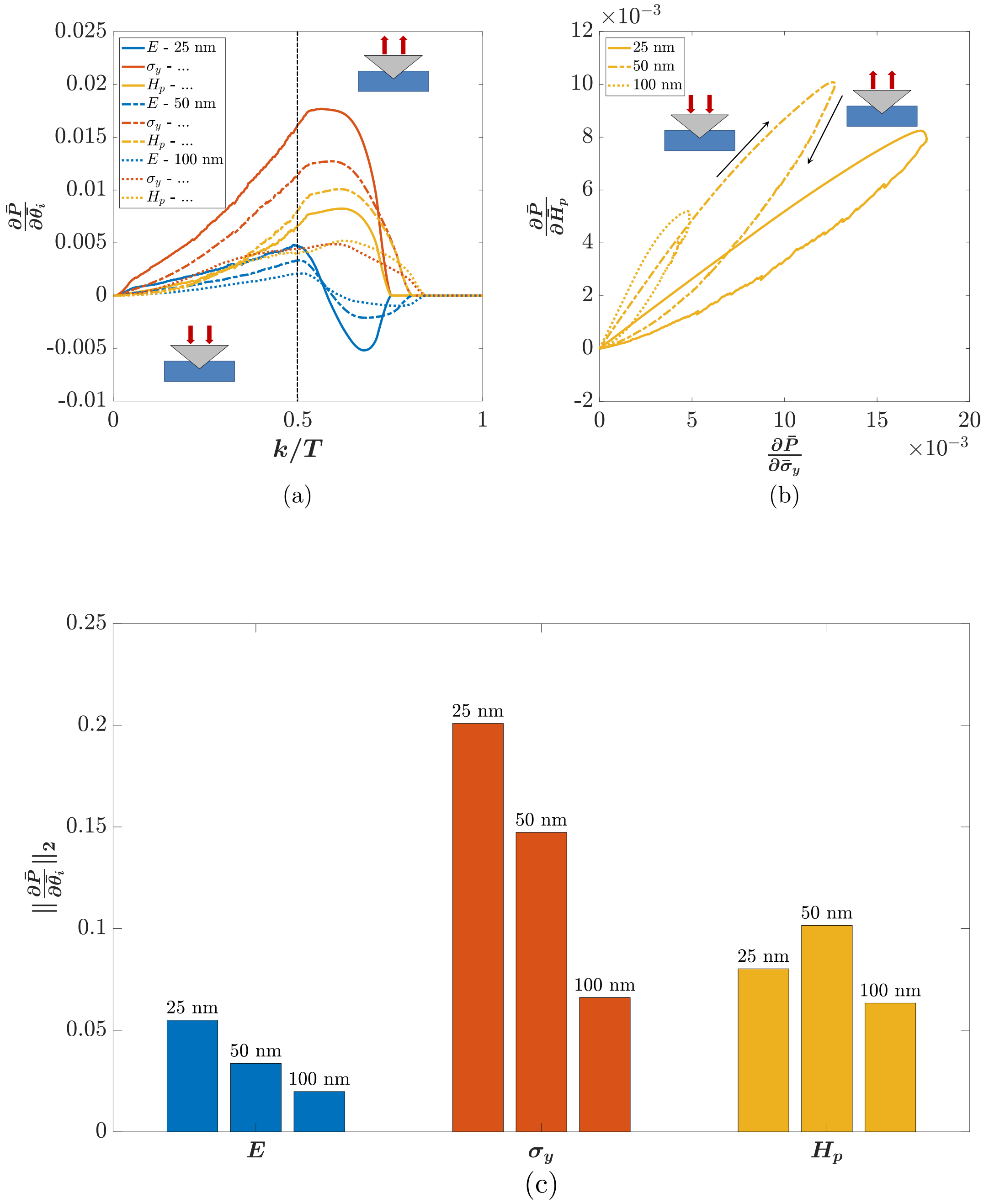

Figure 3: Dimensionless sensitivity of the nanoindentation force to a-perturbation of E, σ_y and H_p for a 25, 50 and 100 nm maximum indentation depth. (a) Evolution of the sensitivity vectors of the nanoindentation force with respect to k/T to a perturbation of E, σ_y and H_p and (b) collinearity between sensitivity vectors of σ_y and H_p. (c) Norm of the dimensionless sensitivity variation of the nanoindentation force to E, σ_y and H_p. A low-pass filter has been applied on the sensitivity vectors for the sake of lisibility to remove the numerical noise.

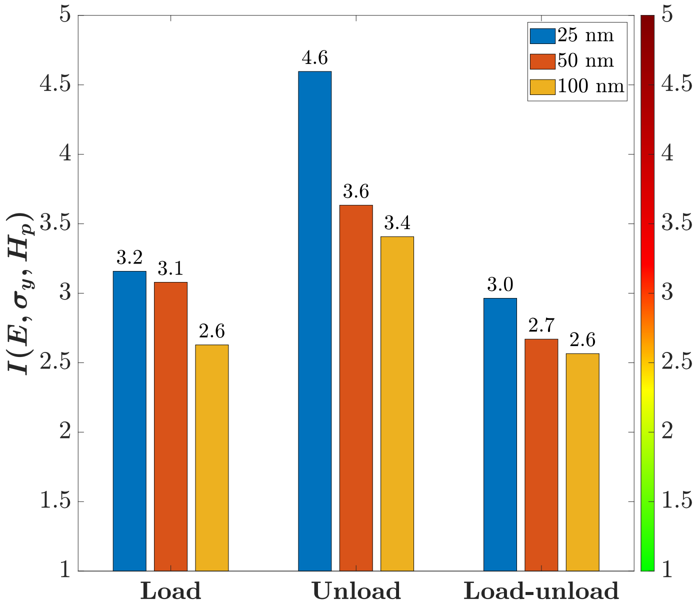

Figure 4: Evolution of the I-index for a 25, 50 and 100 nm maximum indentation depth.

3.1.2. Influence of the indenter tip shape

The identifiability analysis is applied to finite element simulations of a single nanoindentation test using Berkovich and cube corner tips for $h_{max} = 100$ nm.

Figure 5 shows the evolution of the force sensitivity with respect to k/T and the sensitivity norm for a perturbation ϵ of each initial value of E, σ_y and H_p in θ^{01}, as well as the collinearity between sensitivity vectors of σ_y and H_p for the two indenters.

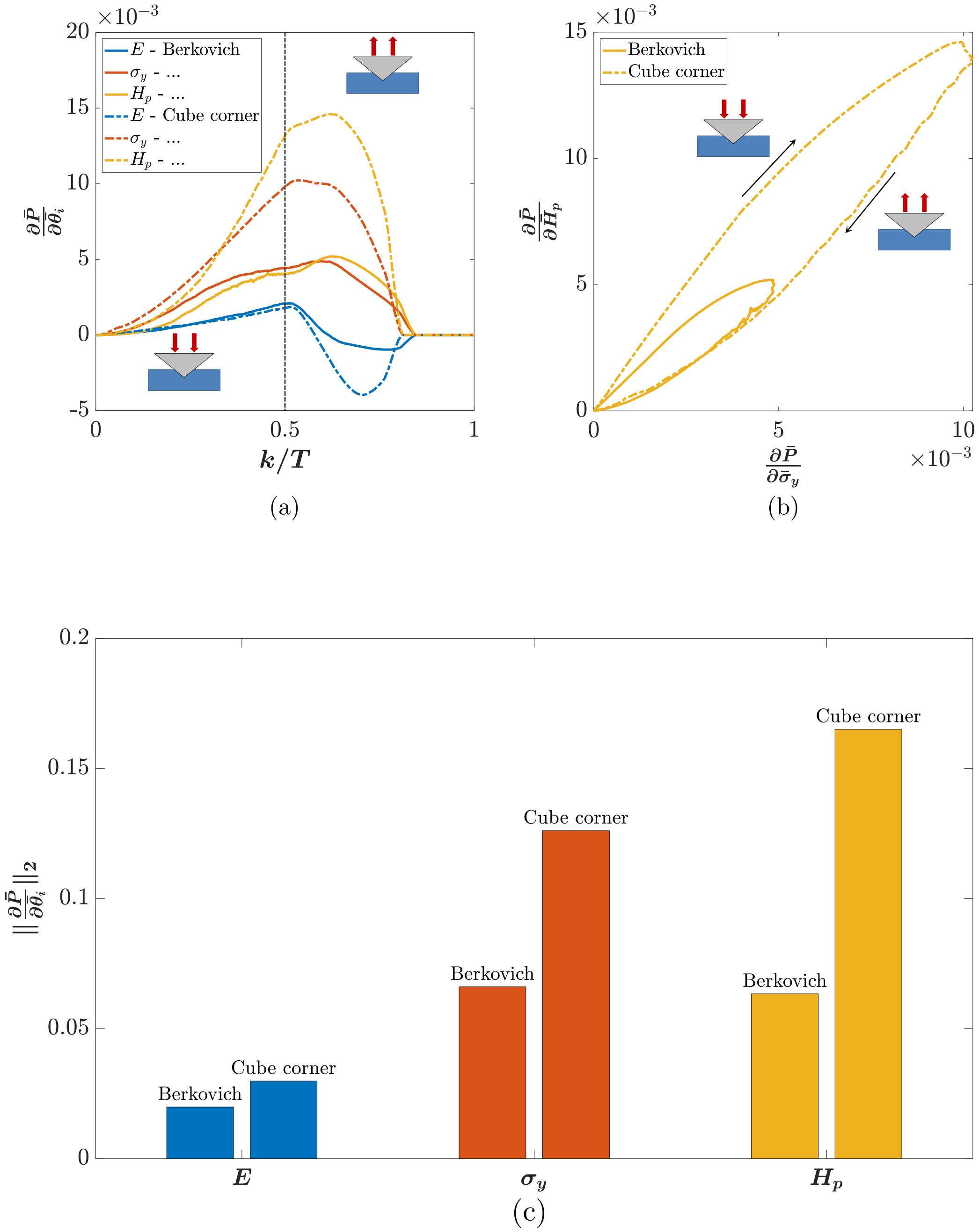

(a) (b)

(c)

Figure 5: Dimensionless sensitivity of the nanoindentation force to a perturbation of E, σ_y and H_p for a 100 nm nanoindentation depth using Berkovich and cube corner tips. (a) Evolution of the sensitivity vectors of the nanoindentation force with respect to k/T ratio to a perturbation of E, σ_y and H_p. and (b) collinearity between sensitivity vectors of σ_y and H_p. (c) Norm of the dimensionless sensitivity variation of the nanoindentation force to E, σ_y and H_p. A low-pass filter has been applied on the sensitivity vectors for the sake of lisibility to remove the numerical noise.

Here, the norm of the sensitivity for E, σ_y and H_p in Figure 5c reveals that using a cube corner tip, the plastic parameters σ_y and H_p are at least twice as much influent on the nanoindentation force than with a Berkovich tip, although these vectors are collinear, up to a multiplicative factor, all along the nanoindentation test, as shown in Figure 5a and Figure 5b. That being said, the much stronger influence of the two plastic parameters over the whole time domain suggest that the cube corner nanoindentation test may have a significant impact on the I-index if the effect of these two variables on the nanoindentation force can be decorrelate, for instance by combining two different tests.

The evolution of $I(E, \sigma_y, H_p)$ is shown in Figure 6, for the two indenters tested. The values of $I(E, \sigma_y, H_p)$ converge to 2.6 and 2.7 and $I(\sigma_y, H_p)$ is equal to 2 and 2.2 respectively for the Berkovich and cube corner experiments, revealing that the problem well-posedness is slightly better with a Berkovich tip. However, all $I(E, \sigma_y, H_p)$ calculations indicates that, as long as a single nanoindentation test is designed, regardless of the nanoindentation depth and the indenter tip, the identification problem of this work, *i.e.* the identification of three parameters E, σ_y and H_p, using the FEMU method is ill-posed and cannot lead to a unique solution.

At this depth (100 nm), the substrate presence is prominent on the mechanical behaviour of the film. Therefore, it is appropriate to exploit its effect by combining two nanoindentation tests, which could variously solicit the substrate with two different indentation depth and two different indenter shape and bring key information to the inverse problem. The next section justifies the choice of experiments to combine, based on the sensitivity analysis achieved in this section and section 3.1.1.

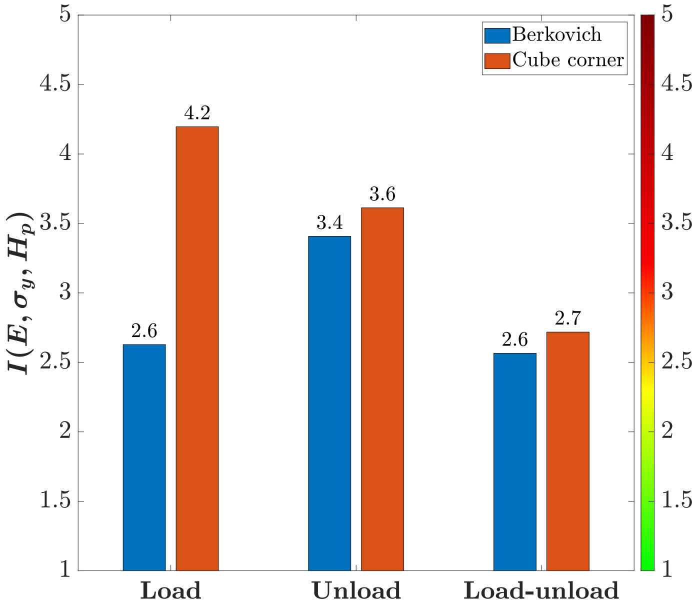

Figure 6: Evolution of the I-index for $h_{max} = 100$ nm using Berkovich and cube corner tips.

3.1.3. Combination of nanoindentation tests

The previous work investigates the influence of the indentation depth and the type of indenter on the identifiability value. The goal here is to investigate the influence of the combination of two different nanoindentation tests, as previous results reveal that one single test is not sufficient to reliably estimate the elastic modulus E and the two plastic parameters (σ_y,H_p) of the film. The main challenge is to dissociate the effect of σ_y and H_p on the nanoindentation force, as the effect of E is already dissociated by the unloading phase of an individual nanoindentation experiment. It is therefore appropriate to combine two experiments with two different indentation depths and two different indenter tips, to bring more information to the inverse problem. A Berkovich experiment at $h_{max} = 50$ nm is a good choice as it gives the strongest influence to H_p and the second highest influence to σ_y compared to the 25 and 100 nm experiments, as shown in Figure 3c. Then, a cube corner experiment at $h_{max} = 100$ nm is likely to help stabilise and decrease the I-index as it brings a high sensitivity of the nanoindentation force to σ_y and H_p, as shown in Figure 5c. This test should allow to activate the substrate effect, also named the anvil effect, and bring key information to identify intrinsic properties of the thin film.

Figure 7 shows the evolution of the force sensitivity with respect to k/T ratio for a perturbation ϵ of each initial value of E, σ_y and H_p in θ^{01}, as well as the collinearity between sensitivity vectors of σ_y and H_p for a 50 nm Berkovich and a 100 nm cube corner experiments. Figure 7b shows that the slope of the sensitivity vector of H_p as a function of the sensitivity vector of σ_y for the 50 nm Berkovich test is lower to that of the 100 nm cube corner test. This difference may break the collinearity between the vectors of σ_y and H_p and improve the value of I-index with a combination of these two tests.

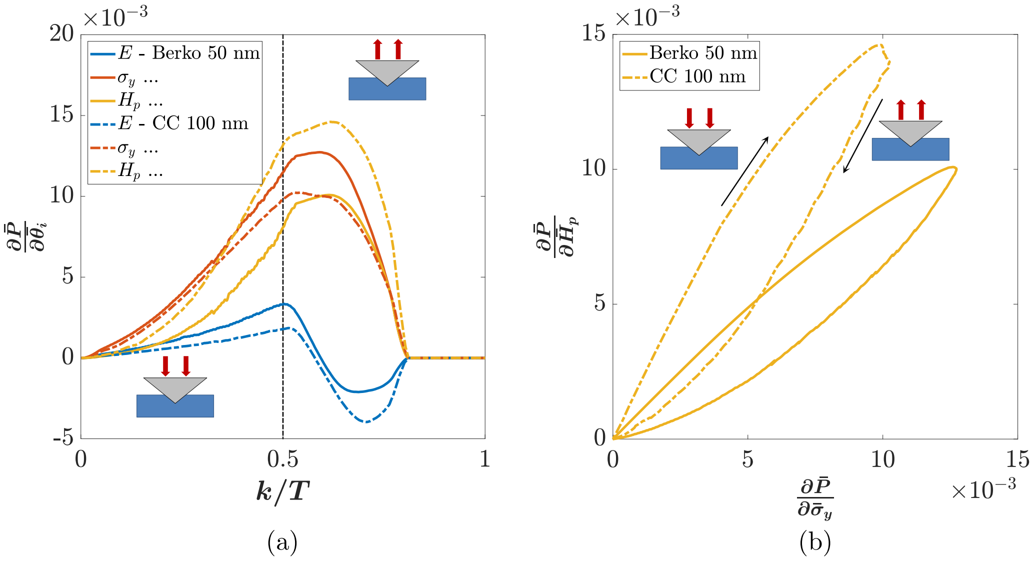

Figure 7: Dimensionless sensitivity of the nanoindentation force to a perturbation of E, σ_y and H_p for a 50 nm Berkovich (Berko) and a 100 nm cube corner (CC) experiments. (a) Evolution of the sensitivity vectors of the nanoindentation force with respect to k/T ratio to a perturbation of E, σ_y and H_p and (b) collinearity between sensitivity vectors of σ_y and H_p. A low-pass filter has been applied on the sensitivity vectors for the sake of lisibility to remove the numerical noise.

Thus, to investigate the influence of the combination of the two nanoindentation tests mentioned above on the I-index value, the quasi-hessian matrix becomes:

$$\bar{H}_{ij} = \sum_{e=1}^{n} \sum_{k=1}^{T} \frac{\partial \bar{P}_k^{(e)}}{\partial \bar{\theta}_i} \frac{\partial \bar{P}_k^{(e)}}{\partial \bar{\theta}_j}, \tag{3.1}$$

with n the number of nanoindentation tests.

The I-index value obtained when combining the two tests is shown in Figure 8. The value of I-index converges to 1.9, confirming that the combination of these two tests improves sufficiently the I-index value to assess the problem well-posedness in the case of this dual nanoindentation experiment. I-index values of loading and unloading phases for each experiment and for the combination of the two also reveals that the two unloading segments of the $P - h$ curves are very complementary and bring key information to the inverse problem, as $I(E, \sigma_y, H_p)$ decreases from 3.6 to 2.0.

What's more, the calculation of $I(\sigma_y, H_p)$ using θ^{01}, reveals that its value decreases from 2.1 and 2.2 for the Berkovich 50 nm and the cube corner 100 nm test respectively, to 1.5 for the combination of the two tests. It shows the complementarity of these two tests to dissociate the influence of the two thin film plastic parameters σ_y and H_p on the force.

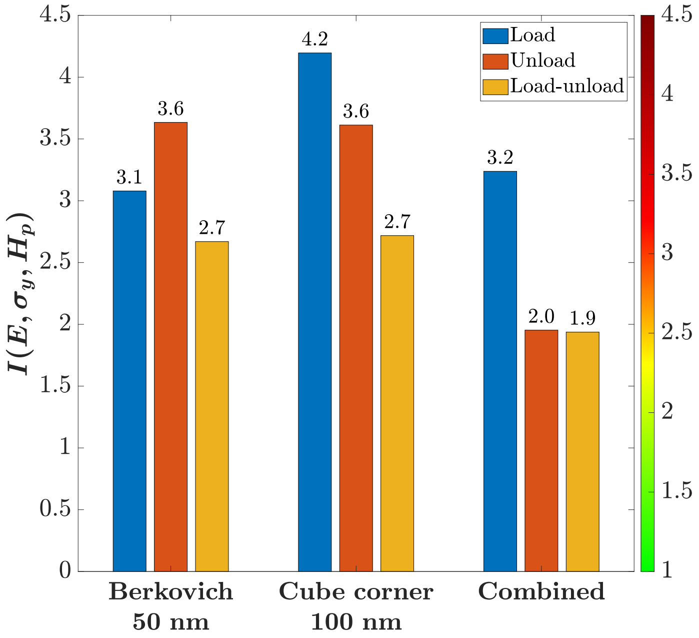

Figure 8: I-index for a combined 50 nm Berkovich and a 100 nm cube corner experiment, compared to the corresponding individual experiments.

3.2. Identification of intrinsic elasto-plastic properties of thin film

This section concerns the identification by the FEMU method of the three thin film elasto-plastic parameters $\theta_1 \equiv E$, $\theta_2 \equiv \sigma_y$ and $\theta_3 \equiv H_p$, with $\theta_4 \equiv \sigma_{ys}$ fixed at 5 GPa (L. Zhang & Mahdi, 1996).

3.2.1. Local identification

The *a priori* identifiability analysis showed that combining a 50 nm Berkovich and a 100 nm cube corner indentation test results in an improvement of the value of I-index, sufficiently low to lead to a well-posed problem. Therefore, the identification procedure is applied to experimental $P-h$ curves obtained from this dual nanoindentation test, from the θ^{01} starting point, which initialise the minimisation process, whose objective function becomes for multiple nanoindentation tests:

$$\omega(\theta) = \frac{1}{2nT}\sum_{e=1}^{n}\sum_{k=1}^{T}\left(\frac{P_k^{(e)}(\theta) - P_k^{exp\,(e)}}{P_{max}^{exp\,(e)}}\right)^2, \tag{3.2}$$

where n is the number of nanoindentation tests, taken as 2 here. The number of acquisition points T is 400, equal for the two tests.

Figure 9 shows the resulting force-displacement curves obtained with the identified parameters $\hat{\theta}^1(E = 198 \text{ GPa}, \sigma_y = 3.6 \text{ GPa}, H_p = 21 \text{ GPa})$ in comparison with the $P - h$ curves for the starting point θ^{01} and the experimental $P - h$ curves from which the optimisation procedure has been applied. It reveals that the optimisation procedure leads to a near match of the experimental and the numerical results, for an objective function which decreases from 7.6×10^{-2} to 9.3×10^{-4}.

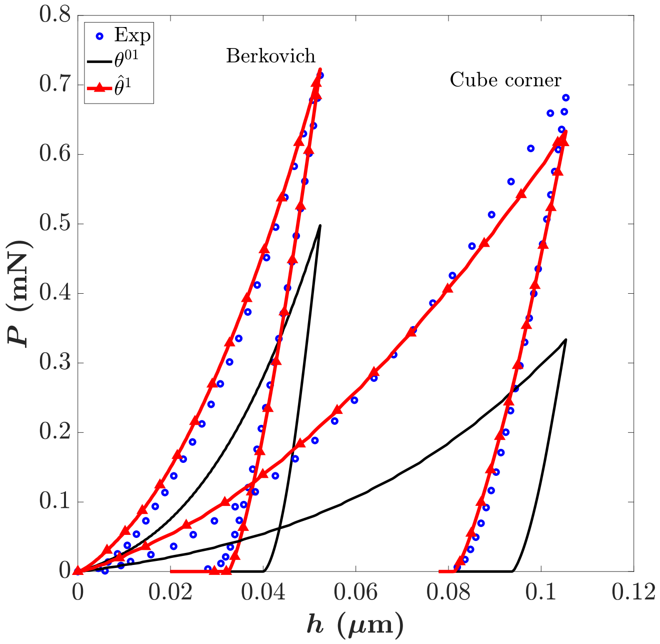

Figure 9: Experimental (Exp) and simulated nanoindentation curves for the θ^{01} starting point and the estimated solution $\widehat{\theta^1}$.

3.2.2. Starting point effect

The identification procedure applied to the designed dual nanoindentation test at the starting point θ^{01}, converge to a unique solution $\hat{\theta}^1$. However, this sole result, and furthermore the optimisation procedure as implemented in this work does not allow to conclude that the solution of the inverse problem is unique. Indeed, there is no restriction of the parameter definition domain assessing the non-existence of local minima.

Therefore, to ensure the robustness of the Levenberg-Marquardt optimisation method in this present work, a set of initial parameters, *i.e.* different starting points, far from each other, has been selected to restrict the presumed order of magnitude of the parameters to identify. This approach ensures that every optimisation paths lead to a unique solution.

Five starting points in the space of the three elasto-plastic parameters E, σ_y and H_p has been selected for the minimisation process so that it ensures a large exploration of the studied space of parameters possibilities. The results of the identification procedure shown in Table 2 and with the corresponding $P - h$ curves in Figure 11 reveals that the five solutions belong to a very restricted domain and regardless of the starting point, the method converge to a minimum $\hat{\theta}(E = 198\text{ GPa}, \sigma_y = 3.6\text{ GPa}, H_p = 21\text{ GPa})$. Therefore, the number of optimisation iterations shown in Figure 10 is the only parameter dependent on the starting point.

Table 2 also indicates *a priori* I-index for each starting points tested for the identification process and reveals that the inverse problem designed with the dual nanoindentation test is *a priori* well-posed for each starting point, except θ^{03}. This difference is discussed in the next section. The I-index computed after the identification process is 1.5. This confirms the quality of the solution.

Starting points	Parameters θ_j			Objective function ω	I-index
	θ_1 E (GPa)	θ_2 σ_y (GPa)	θ_3 H_p (GPa)		
θ^{01}	200	1	5	$3.8\text{x}10^{-2}$	1.9
$\hat{\theta}^{1}$	199	3.5	21	$4.7\text{x}10^{-4}$	1.5
θ^{02}	200	5	50	$9.0\text{x}10^{-3}$	1.5
$\hat{\theta}^{2}$	198	3.6	21	$4.7\text{x}10^{-4}$	1.5
θ^{03}	200	8.7	2	$2.0\text{x}10^{-3}$	3.3
$\hat{\theta}^{3}$	198	3.6	21	$4.7\text{x}10^{-4}$	1.5
θ^{04}	300	3	30	$1.3\text{x}10^{-3}$	1.6
$\hat{\theta}^{4}$	198	3.6	21	$4.7\text{x}10^{-4}$	1.5
θ^{05}	100	2	10	$1.1\text{x}10^{-2}$	1.7
$\hat{\theta}^{5}$	199	3.5	21	$4.7\text{x}10^{-4}$	1.5

Table 2: Estimated parameters set $\hat{\theta}$ from the identification procedure using five starting points.

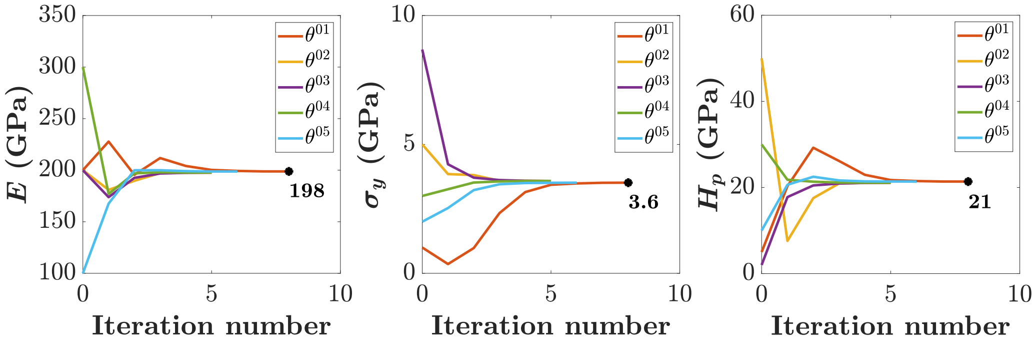

Figure 10: Evolution of the parameters E, σ_y and H_p during the identification procedure using five starting points.

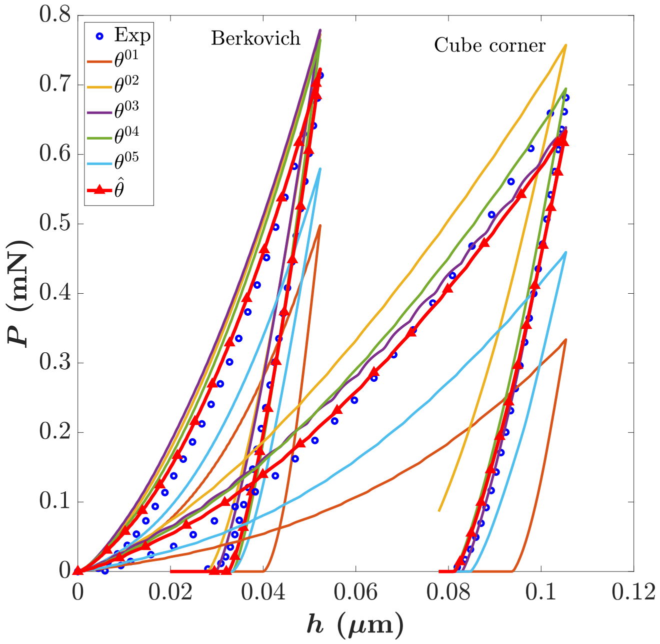

Figure 11: Experimental and simulated nanoindentation curves for the five starting points and the estimated solution $\hat{\theta}$.

3.2.3. On the activation of the substrate effect

The dual experiment designed in this work rely upon the activation of the substrate effect, or anvil effect (Y. Zhang et al., 2015).

Multiple nanoindentation tests on a bulk material with the same indenter geometry at different indentation depths (in the same order of the indentation depths studied in this work) are homothetic. This leads notably to a constant h_c/h_{max} ratio between the tests, h_c being the indentation depth after which the indenter is no longer in contact with the sample. In the case of a coated material, h_c/h_{max} is going to evolve with the indentation depth as the properties of the composite material substrate-coating vary with the indentation depth. This is called the anvil effect. In the case of a composite material substrate-coating, it is thus appropriate to exploit this phenomenon by varying the indenter depth and amplify it by changing the indenter tip shape.

I-index allows the measurement of the information richness brought by experiments to quantify the ill or well-posedness of the inverse problem. To understand where significant information is located during the test, Figure 12 represents the evolution of *a priori* I-index during the dual nanoindentation test for the five starting points.

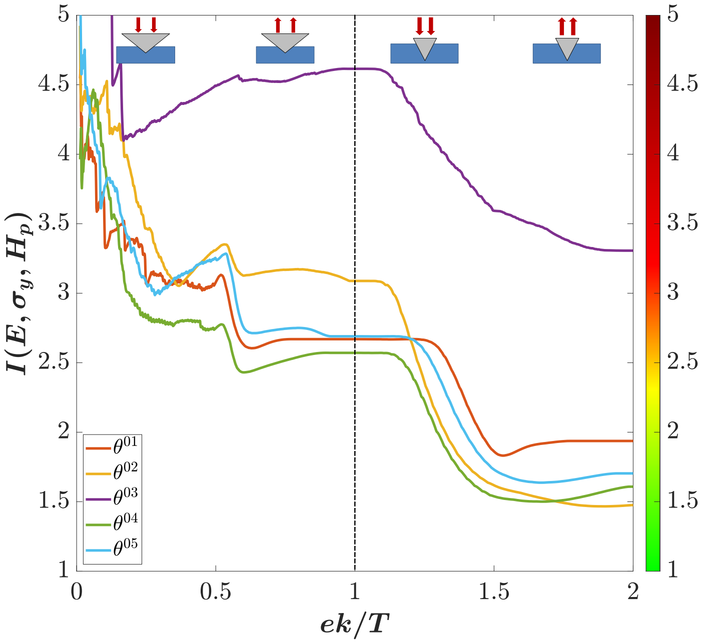

Figure 12: Evolution of I-index for the five starting points with respect to k/T ratio where $k/T = 1$ and $k/T = 2$ are respectively the ends of the 50 nm Berkovich and 100 nm cube corner experiments.

The highest decrease of I-index, which is correlated with a gain of information, occurs during the loading phase of the cube corner test for each starting point. To illustrate physically this gain of information, Figure 13 shows the equivalent plastic strain fields at maximum depth for the 50 nm Berkovich and 100 nm cube corner experiments using θ^{01}. It reveals that plastic deformation occurs in the substrate during the cube corner loading phase, and not during the Berkovich test, which coincides with the I-index decrease observed from $ek/T = 1.2$ to 1.5.

Therefore, this difference of plastic deformation exhibited by the combination of these two tests allows to sufficiently decrease I-index value to lead to a well-posed problem. It reflects the complementarity of these two tests and that the effect of each parameter on the force has been dissociated, in particular the effect of σ_y and H_p. Indeed, the dissociation of the effect of E is already brought by the unloading phase, as shown in Figure 7a. Therefore, the exacerbation of the anvil effect by switching to a cube corner tip mostly benefit to the dissociation of the influence of σ_y and H_p on the force.

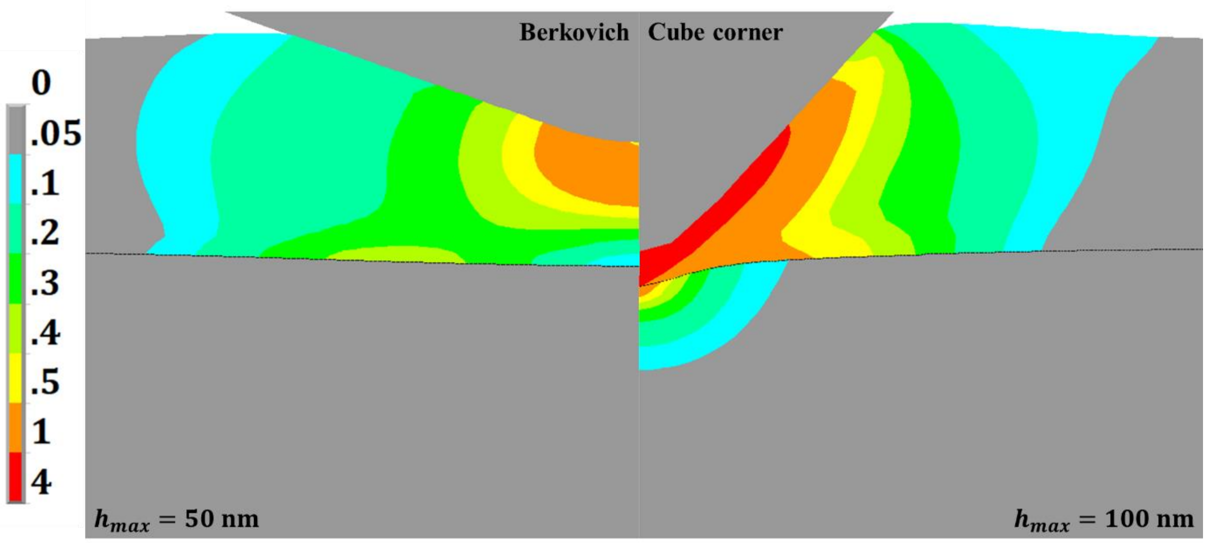

Figure 13: Equivalent plastic strain fields at maximum depth for the 50 nm Berkovich and 100 nm cube corner experiments using the θ^{01} starting point.

In the particular case of θ^{03}, the same decrease of I-index occurs during the cube corner loading phase, but still not reaching a sufficiently low I-index value to interpret this as a well-posed problem. Indeed, the low H_p value ($H_p = 2$ GPa) induces a low sensitivity of the nanoindentation force to this parameter. This leads to a bad I-index, although θ^{03} allow the activation of the anvil effect, as shown in Figure 14, allowing its convergence to the same solution $\hat{\theta}(E = 198\ \text{GPa}, \sigma_y = 3.6\ \text{GPa}, H_p = 21\ \text{GPa})$.

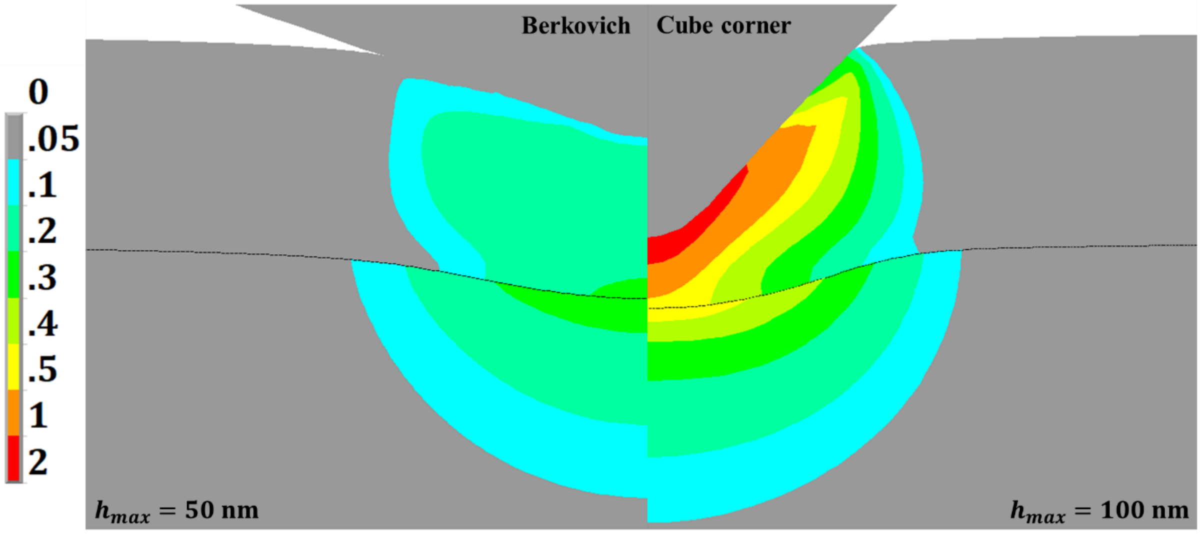

Figure 14 : Equivalent plastic strain fields at maximum depth for the 50 nm Berkovich and 100 nm cube corner experiments using the θ^{03} starting point.

The equivalent plastic strain field of the 100 nm cube corner experiment reveals that the substrate plastically deforms. Therefore, by soliciting sufficiently the substrate to engage its plastic deformation, it should allow the dissociation of the substrate plasticity, driven by its yield stress σ_{ys}, from the thin film elastoplastic behaviour. This is even truer given the fact that I-index evolution is similar for each starting point, with a significative decrease during the cube corner phase. This results in a non-zero sensitivity of the nanoindentation force to σ_{ys} and a decoupling of the influence of this parameter on the force from the thin film elastoplastic parameters.

Therefore, it is worth considering the identification of σ_{ys}, previously assumed in the finite element model, on top of the thin film elasto-plastic parameters. All the more so that, as stated in section 3.2.2, I-index computed after the identification process, is 1.5 < 2, indicating a margin of information brought by the dual nanoindentation test. It is thus appropriate to define a new starting point θ^0 from the previous identified value of $E = 198$ GPa $(\hat{\theta}_1)$, $\sigma_y = 3.6$ GPa $(\hat{\theta}_2)$ and $H_p = 21$ GPa $(\hat{\theta}_3)$, including the substrate yield stress $\sigma_{ys} = 5$ GPa (θ_4), to exploit the margin of information at this starting point to study the influence of the inclusion of σ_{ys} in the minimisation process.

3.3. Inclusion of the substrate yield stress in the identification process

In this section, the hypothesis $\sigma_{ys} = 5$ GPa is released and this parameter is included in the identification process.

3.3.1. *A priori* identifiability analysis

The sensitivity norms of E, σ_y, H_p and σ_{ys}, is first computed using $\theta^0(E = 198 \text{ GPa}, \sigma_y = 3.6 \text{ GPa}, H_p = 21 \text{ GPa}, \sigma_{ys} = 5 \text{ GPa})$ to investigate how sensitive is the force from the dual nanoindentation test to each parameter, mainly to the substrate yield stress σ_{ys}, as it needs to be enough influent to be identified by the updating process.

Figure 15 validates this necessity, with σ_{ys} having the strongest influence on the force response for both the 50 nm Berkovich and 100 nm cube corner experiments.

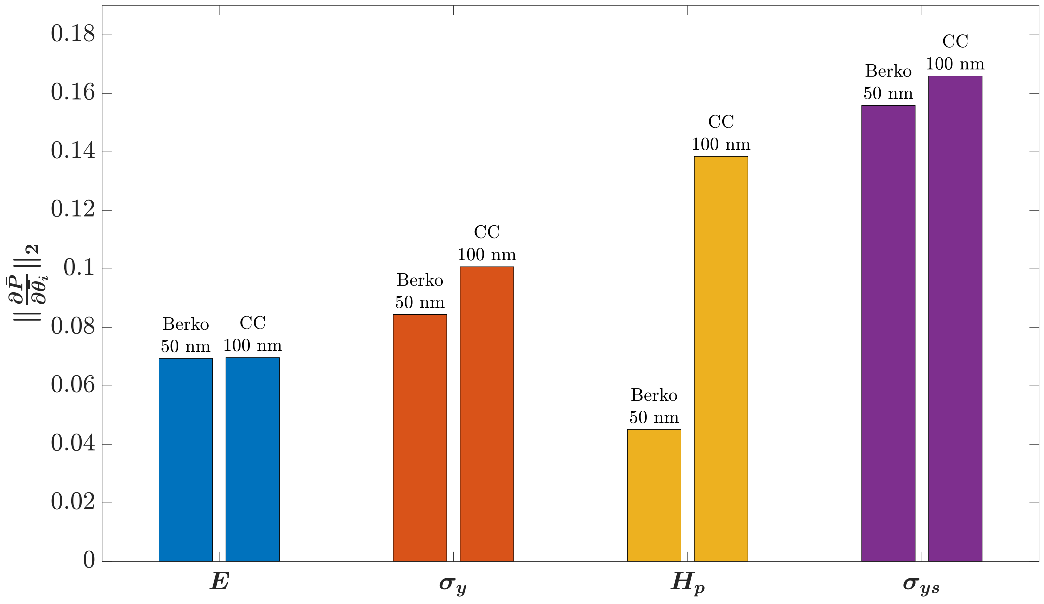

Figure 15: Norm of the sensitivity variation of the nanoindentation force to a perturbation of E, σ_y, H_p and σ_{ys} for a 50 nm Berkovich (Berko) and 100 nm cube corner (CC) experiment.

The value of $I(E, \sigma_y, H_p, \sigma_{ys})$ obtained for this dual nanoindentation experiment, in the case of the perturbation of the four parameters E, σ_y, H_p and σ_{ys} shown in Figure 16 is 2.1, higher than $I(E, \sigma_y, H_p) = 1.5$ with a perturbation of only the three parameters of the thin film, however still sufficiently low to ensure a reliable identification of the four parameters of the inverse problem. Indeed, the inclusion of a highly influent parameters σ_{ys} has limited the increase of the I-index, which otherwise would have been occurred with the inclusion of a fourth unknown parameter. Moreover, Figure 16 reveals that the two experiments are very complementary as their combination help stabilise $I(E, \sigma_y, H_p, \sigma_{ys})$ from about 3.8-3.9, describing a large space of parameter possibilities with high uncertainties, to 2.1, reflecting a well-posed problem where each optimisation paths are susceptible to converge to a unique solution.

I-index values of loading and unloading phases for each experiment and for the combination of the two reveal that the exploitation of the whole $P - h$ curves is mandatory to expect to identify the four parameters, as $I(E, \sigma_y, H_p, \sigma_{ys})$ only sufficiently decreases when the two loading and unloading segments are taken into account. What's more, $I_{loads}(E, \sigma_y, H_p) = 2.3$ whereas $I_{unloads}(E, \sigma_y, H_p) = 1.4$ meaning that it is possible to identify E, σ_y and H_p of the film knowing σ_{ys} with the two unloading phases, as also shown in Figure 8. Thus, the margin of information, which should allow to identify the substrate yield stress σ_{ys} on top of the 3 thin film parameters, is arguably brought by the loading phase of each experiment.

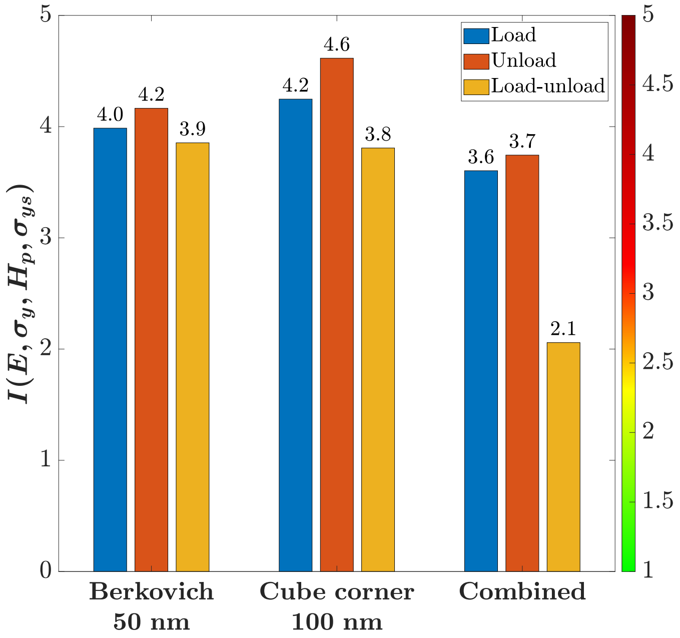

Figure 16: I-index for four unknown parameters E, σ_y, H_p and σ_{ys} for a combined 50 nm Berkovich and a 100 nm cube corner experiment, compared to the I-index of the corresponding individual experiments.

3.3.2. Simultaneous identification of the four parameters

The identification procedure using FEMU method is applied to the experimental $P-h$ curves obtained from the dual nanoindentation test using the starting point $\theta^0(E = 198\ \text{GPa}, \sigma_y = 3.6\ \text{GPa}, H_p = 21\ \text{GPa}, \sigma_{ys} = 5\ \text{GPa})$, thus defined by the previous set of identified parameters of the thin film and the substrate yield stress assumed previously in the finite element model.

Figure 17 shows the resulting force-displacement curves obtained with the identified parameters $\hat{\theta}_f(E = 211\ \text{GPa}, \sigma_y = 2\ \text{GPa}, H_p = 22\ \text{GPa}, \sigma_{ys} = 6.4\ \text{GPa})$ in comparison with the $P-h$ curves for the starting point θ^0 and the experimental $P-h$ curves from which the optimisation procedure has been applied. It reveals that the optimisation procedure leads to an even better match of the experimental and numerical results, for an objective function which improves from 4.7×10^{-4} to 3.7×10^{-4}.

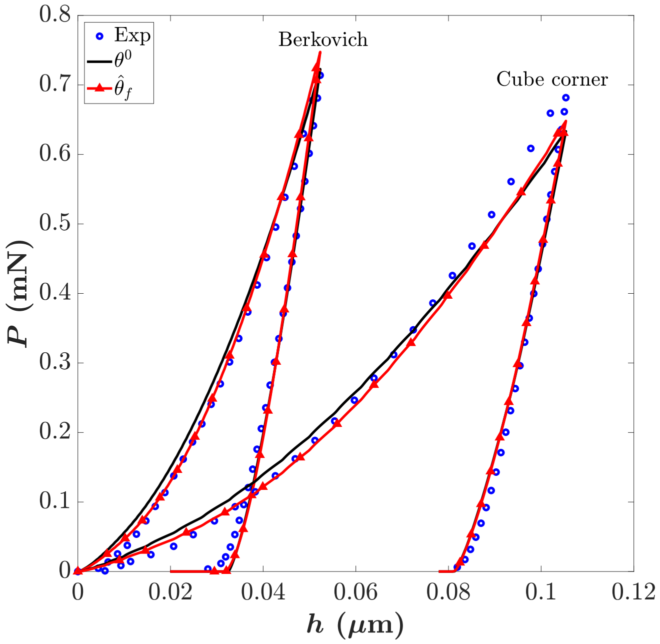

Figure 17: Experimental and simulated nanoindentation curves for the starting point $\theta^0$and the estimated solution $\hat{\theta}_f$.

A posteriori I-index calculated at the final solution $\hat{\theta}_f$ is 2.1, proving the local stability of the final solution. However, just as for the first identification conducted in section 3.2.1, this sole identification result does not prove that the founded solution $\hat{\theta}_f$ is unique.

Therefore, to ensure the robustness of the Levenberg-Marquardt algorithm (section 3.2.2), an identification procedure has been conducted using the five initial starting points θ^{01} to θ^{05} reported in Table 1 while releasing the substrate yield stress with an initial value of 5 GPa in each starting points. The evolution of each parameters E, σ_y, H_p and σ_{ys} during the minimisation process from each starting points shown in Figure 18 reveals that each optimisation paths converge to the same solution $\hat{\theta}_f(E = 211\ \text{GPa}, \sigma_y = 2\ \text{GPa}, H_p = 22\ \text{GPa}, \sigma_{ys} = 6.4\ \text{GPa})$, indicating that the starting point does not influence the result. In that respect, it can be concluded that the final solution is unique.

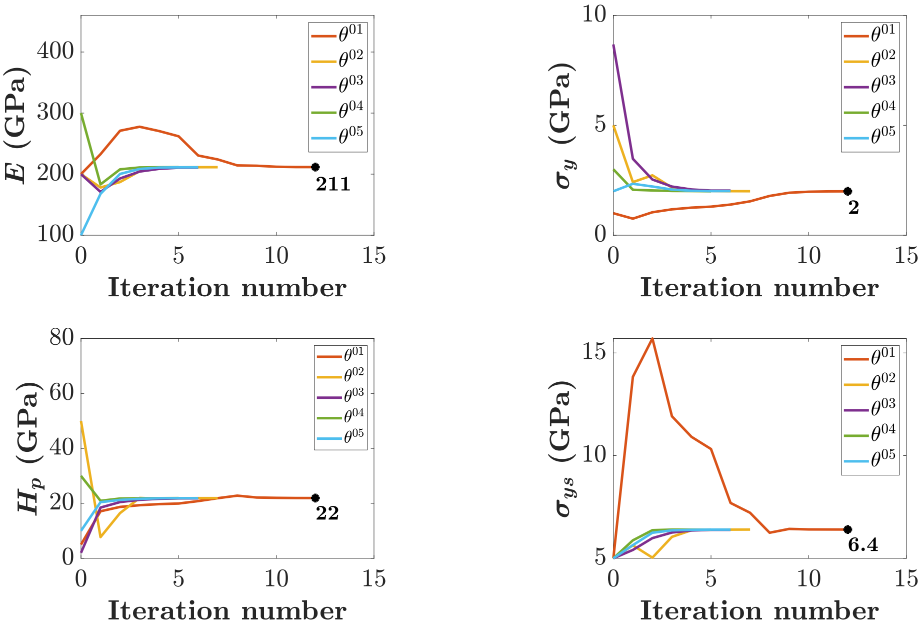

Figure 18: Evolution of the parameters E, σ_y, H_p and σ_{ys} during the identification procedure using five starting points.

Figure 19 represents the stress-strain curves of the identified elasto-plastic behaviour of the thin film before $(\hat{\theta}(E = 198\ \text{GPa}, \sigma_y = 3.6\ \text{GPa}, H_p = 21\ \text{GPa}))$ and after $(\hat{\theta}_f(E = 211\ \text{GPa}, \sigma_y = 2\ \text{GPa}, H_p = 22\ \text{GPa}))$ the inclusion of the substrate yield stress in the identification process. The relative error on the three elastoplastic parameters of the film, without its inclusion, is – 6.2%, 80% and – 4.5% respectively for E, σ_y and H_p. It shows that the substrate effect has a significant influence on the plastic behaviour of the film and on the accuracy of the film yield stress estimation.

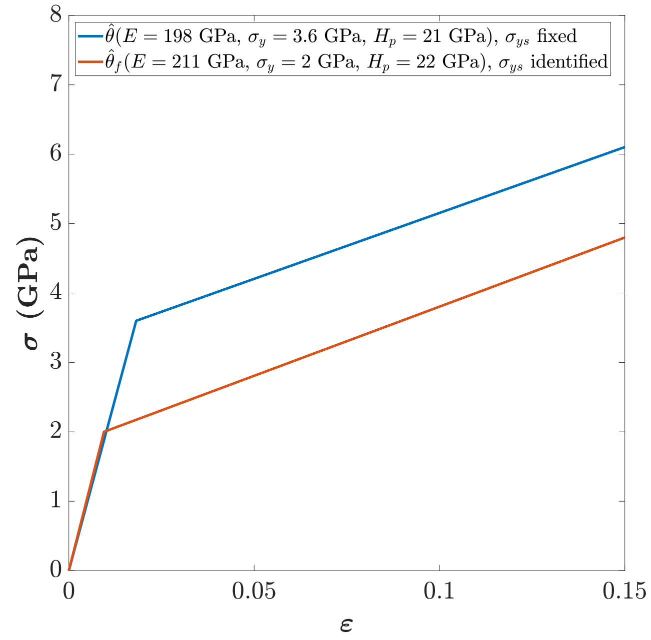

Figure 19: Stress-strain curves describing the identified elasto-plastic behaviour of the thin film before ($\hat{\theta}$) and after ($\hat{\theta}_f$) the inclusion of the substrate yield stress in the identification process.

3.4. Validation of the estimated parameters

In this section, the validation of the set of identified parameters is done by confronting: (i) the numerical and experimental $P - h$ curves of a nanoindentation test on the bulk silicon substrate and (ii) the numerical and experimental topography of the imprint of a nanoindentation test on the composite alumina thin film - silicon substrate sample.

3.4.1. Validation using a silicon nanoindentation curve

The identified value of σ_{ys} is validated here with a direct simulation of a force-controlled Berkovich nanoindentation test at $P_{max} = 5$ mN on the silicon substrate using the same 2D-axissymetric model geometry and mesh presented in section 2.3, but without the thin film mesh.

Figure 20 shows the simulated $P - h$ curve obtained with the identified value of $\sigma_{ys} = 6.4$ GPa, compared to the $P - h$ curve for the previously assumed value of $\sigma_{ys} = 5$ GPa. It reveals a better match between the numerical and the experimental results and confirms the completeness of the method exposed in this work, from the design of experiments to the following simultaneous identification of the elasto-plastic parameters of the alumina thin film and the silicon yield stress. Note that the noticeable slope discontinuity at the end of the unloading part of the experimental curve is due to the phase transition of silicon (S. Wang et al., 2017) which is not considered in the finite element model of the nanoindentation test.

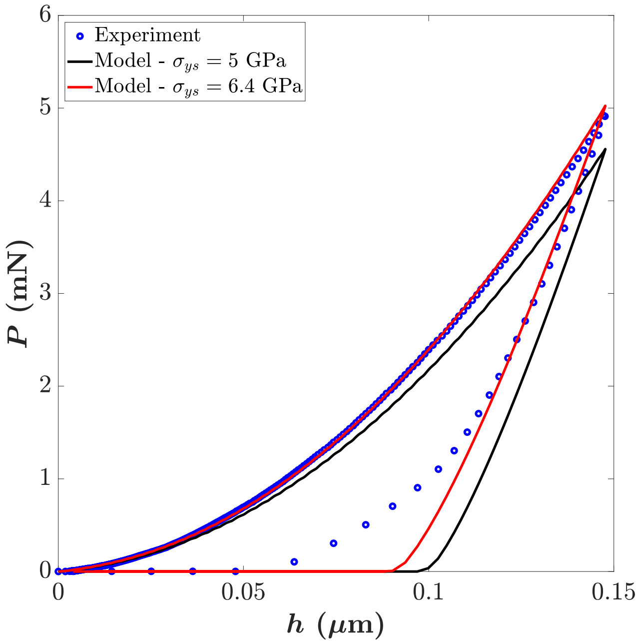

Figure 20 : Experimental and simulated $P-h$ curves for $\sigma_{ys}=6.4$ GPa and $\sigma_{ys}=5$ GPa of a nanoindentation test on silicon.

3.4.2. Validation using residual topographies and 3D FEM

The identified parameter values in $\hat{\theta}_f(E=211\text{ GPa}, \sigma_y=2\text{ GPa}, H_p=22\text{ GPa}, \sigma_{ys}=6.4\text{ GPa})$ are validated using the imprint of a force controlled Berkovich nanoindentation test at $P_{max}=5$ mN on the composite alumina thin film-substrate sample. A 3D FEM of the nanoindentation test is built in this instance to accurately simulate the pile-up area around the imprint. This model is detailed in section 2.3.2.

The nanoindentation $P-h$ curve obtained using the 3D FEM is compared to the experimental $P-h$ curve and the one from the 2D axisymmetric FEM, as shown in Figure 21. It reveals that the 3D model of the nanoindentation test is in accordance with the 2D axisymmetric model, meaning that the use of the 2D axisymmetric model in this study is convenient to reliably simulate trends of experimental observations from a nanoindentation test.

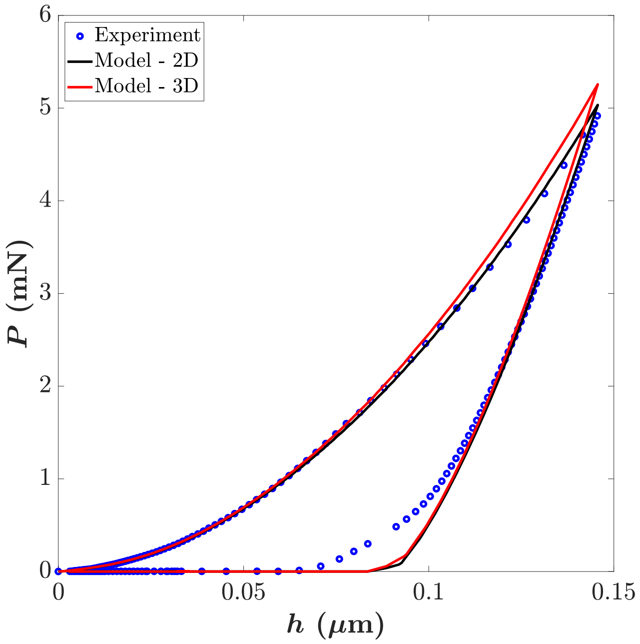

Figure 21: Experimental and simulated $P-h$ curves using the 2D axisymmetric and the 3D finite element model of a Berkovich nanoindentation test on the composite system thin film – substrate.

Experimental Atomic Force Microscopy (AFM) topography and simulated residual topography of the Berkovich nanoindentation test are shown in Figure 22. The simulated residual imprint is very similar to the experimental imprint in terms of shape and size. The pile-up distribution around the imprint is comparable, and furthermore the pile-up ratio Z/h_{max} is of the same order of magnitude, although a slight difference in pile-up ratio is discernible between the two topographies. This is due to the overestimation of the numerical residual depth h_r, leading to higher pile-ups for the numerical topography, as the phase transition of silicon, related to the slope discontinuity visible on the experimental $P-h$ curve in Figure 21, is not modelled in the 3D FEM.

Thus, this comparison consolidates the preceding validation made with a silicon nanoindentation curve concerning the estimated values of $\hat{\theta}_f(E = 211\text{ GPa}, \sigma_y = 2\text{ GPa}, H_p = 22\text{ GPa}, \sigma_{ys} = 6.4\text{ GPa})$ and the completeness of the method exposed in this work.

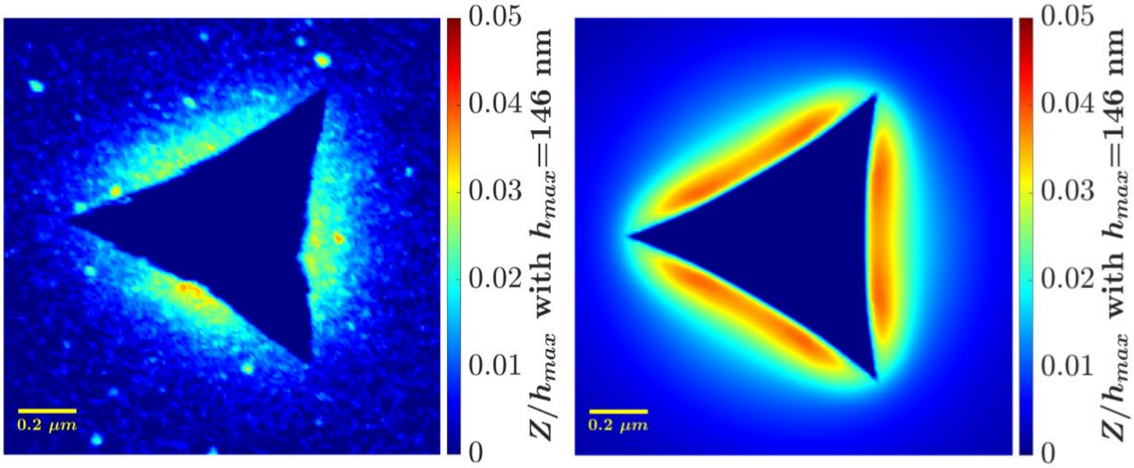

Figure 22: Experimental AFM topography and simulated residual topography using the 3D FEM of a nanoindentation test on the composite system thin film ($e_f = 100$ nm) – substrate at $h_{max} = 146$ nm. The topography values Z are normalised by the maximum indentation depth h_{max}. Pile-ups are highlighted by adapting the color code to only consider the matter above zero.

In addition, estimated values of E and σ_y for the alumina thin film have been compared with values in literature. Tripp *et al.* have extracted the intrinsic elastic modulus of a 100 nm alumina thin film deposited by ALD from membrane bulge testing, obtaining a value of around 180 ± 20 GPa (Tripp et al., 2006), which is in accordance with the identified value of 211 GPa. Using experimental and numerical simulations of nanoindentation tests, Pelletier *et al.* have estimated a yield stress for amorphous alumina deposited on silicon substrate comprised between 1.5 to 3 GPa, depending on the film thickness (from 250 nm to 1000 nm) and assuming a substrate yield stress of 4 GPa (Pelletier et al., 2006). They have used the same bilinear elasto-plastic law assumption (section 2.2). However, it is worth noting that some elements of the Pelletier *et al.* study differ from this present work: (i) alumina deposition has been processed by evaporation, and (ii) assuming a low hardening for nanoindentation simulations, on the order of $EH_p/(E + H_p) = E/1000$. Also, the method used to estimate this parameter is different, as it fits only the loading phase of experimental and numerical nanoindentation test with a polynomial function for different σ_y/σ_{ys} ratios, with fixed $E/E_{substrate} = 0.7$. Nevertheless, this comparison gives an order of magnitude in accordance with the estimated value of 2 GPa of this present work.

4. Conclusion

The goal of this work was to evaluate the possibility to estimate the elasto-plastic parameters of an alumina thin film (Young modulus E, yield stress σ_y and hardening modulus H_p) and the silicon substrate plasticity (yield stress σ_{ys}) using outputs provided by nanoindentation $P-h$ curves. The method implemented here attempts to target *a priori* the experiments to realized experimentally to ensure a reliable identification of the parameters using the FEMU method. The use of an identifiability indicator (I-index) allowed to quantify the information brought by experiments by reflecting the stability of the inverse problem potential solution, *i.e.*, its sensitivity to a perturbation on the nanoindentation force. The key conclusions of this work are as follows:

- I-index calculations helped design a judicious combination of experiments, involving two indenter tip shapes with wisely selected maximum indentation depths.
- The identification procedure using the FEMU method applied to the designed dual nanoindentation experiment led to a unique solution, *i.e.* not sensitive to the starting point of the optimisation method, leading to a good fit between numerical and experimental $P-h$ curves. Moreover, the calculation of *a posteriori* I-index assessed the stability of the found solution and thus, with the uniqueness and stability verified, the quality of the solution. This confirms the proper working and the interest of an *a priori* numerical design of experiments based on identifiability in the case of a composite system thin film-substrate.
- The anvil effect exhibited by this dual tip experiment allowed to identify the substrate yield stress on top of the three thin film elasto-plastic parameters, *i.e.* its Young's modulus, yield stress and hardening modulus.
- The three true intrinsic elastoplastic parameters of the thin film can only be obtained by including the substrate yield stress in the FEMU method. Indeed, the relative error on the three elastoplastic parameters of the film, without its inclusion, is – 6.2%, 80% and – 4.5% respectively for E, σ_y and H_p. It demonstrates the significant influence of the substrate on the plastic behaviour of the film and on the accuracy of the estimation of the film properties, especially the yield stress σ_y. Therefore, the thin film – substrate configuration is very profitable for the reliable estimation of the three elastoplastic parameters of the film and the substrate yield stress ($E = 211\ \text{GPa}, \sigma_y = 2\ \text{GPa}, H_p = 22\ \text{GPa}, \sigma_{ys} = 6.4\ \text{GPa}$) with the FEMU method, with judiciously designed nanoindentation experiments.

Besides this approach uses nanoindentation experiments exclusively, *i.e.* only $P-h$ curves without the imprint topography or profile. Thus, it allows a simple experimental implementation without the need of AFM which permits limited handling and carefulness steps prior to the test. Lastly, the development of a robust identification method, as established in this work, provide the opportunity to assess the evolution of intrinsic parameters: E, σ_y and H_p in function of annealing conditions of the alumina thin film.

Acknowledgement

This work has been funded by the French National Research Agency (ANR) & DGA Defense Innovation Agency (AID).

References

Alkorta, J., Martínez-Esnaola, J. M., & Sevillano, J. G. (2005). Absence of one-to-one correspondence between elastoplastic properties and sharp-indentation load–penetration data. *Journal of Materials Research*, *20*(2), 432–437. https://doi.org/10.1557/JMR.2005.0053

Anstett-Collin, F., Denis-Vidal, L., & Millérioux, G. (2020). A priori identifiability: An overview on definitions and approaches. *Annual Reviews in Control*, *50*, 139–149. https://doi.org/10.1016/j.arcontrol.2020.10.006

Bec, S., Tonck, A., Georges, J.-M., Georges, E., & Loubet, J.-L. (1996). Improvements in the indentation method with a surface force apparatus. *Philosophical Magazine A*, *74*(5), 1061–1072. https://doi.org/10.1080/01418619608239707

Bec, S., Tonck, A., & Loubet, J. L. (2006). A simple guide to determine elastic properties of films on substrate from nanoindentation experiments. *Philosophical Magazine*, *86*(33–35), 5347–5358. https://doi.org/10.1080/14786430600660856

Bei, H., George, E. P., Hay, J. L., & Pharr, G. M. (2005). Influence of Indenter Tip Geometry on Elastic Deformation during Nanoindentation. *Physical Review Letters*, *95*(4), 045501. https://doi.org/10.1103/PhysRevLett.95.045501

Bocciarelli, M., & Bolzon, G. (2009). Indentation and imprint mapping for the identification of interface properties in film-substrate systems. *International Journal of Fracture*, *155*(1), 1–17. https://doi.org/10.1007/s10704-009-9314-y

Bocciarelli, M., Bolzon, G., & Maier, G. (2005). Parameter identification in anisotropic elastoplasticity by indentation and imprint mapping. *Mechanics of Materials*, *37*(8), 855–868. https://doi.org/10.1016/j.mechmat.2004.09.001

Bocciarelli, M., Bolzon, G., & Maier, G. (2008). A constitutive model of metal–ceramic functionally graded material behavior: Formulation and parameter identification. *Computational Materials Science*, *43*(1), 16–26. https://doi.org/10.1016/j.commatsci.2007.07.047

Bolzon, G., Bocciarelli, M., & Chiarullo, E. J. (2009). Mechanical Characterization of Materials by Micro-Indentation and AFM Scanning. In B. Bhushan & H. Fuchs (Eds.), *Applied Scanning Probe Methods XII* (pp. 85–120). Springer Berlin Heidelberg. https://doi.org/10.1007/978-3-540-85039-7_5

Bolzon, G., Buljak, V., Maier, G., & Miller, B. (2011). Assessment of elastic–plastic material parameters comparatively by three procedures based on indentation test and inverse analysis. *Inverse Problems in Science and Engineering*, *19*(6), 815–837. https://doi.org/10.1080/17415977.2011.551931

Bolzon, G., Maier, G., & Panico, M. (2004). Material model calibration by indentation, imprint mapping and inverse analysis. *International Journal of Solids and Structures*, *41*(11–12), 2957–2975. https://doi.org/10.1016/j.ijsolstr.2004.01.025

Bucaille, J. L., Stauss, S., Felder, E., & Michler, J. (2003). Determination of plastic properties of metals by instrumented indentation using different sharp indenters. *Acta Materialia*, *51*(6), 1663–1678. https://doi.org/10.1016/S1359-6454(02)00568-2

Cai, X., & Bangert, H. (1995). Hardness measurements of thin films-determining the critical ratio of depth to thickness using FEM. *Thin Solid Films*, *264*(1), 59–71. https://doi.org/10.1016/0040-6090(95)06569-5

Cao, Y. P., & Lu, J. (2004). Depth-sensing instrumented indentation with dual sharp indenters: Stability analysis and corresponding regularization schemes. *Acta Materialia*, *52*(5), 1143–1153. https://doi.org/10.1016/j.actamat.2003.11.001

Capehart, T. W., & Cheng, Y.-T. (2003). Determining constitutive models from conical indentation: Sensitivity analysis. *Journal of Materials Research*, *18*(4), 827–832. https://doi.org/10.1557/JMR.2003.0113

Casals, O., & Alcalá, J. (2005). The duality in mechanical property extractions from Vickers and Berkovich instrumented indentation experiments. *Acta Materialia*, *53*(13), 3545–3561. https://doi.org/10.1016/j.actamat.2005.03.051

Cheng, L., Xia, X., Yu, W., Scriven, L. E., & Gerberich, W. W. (2000). Flat-punch indentation of viscoelastic material. *Journal of Polymer Science Part B: Polymer Physics*, *38*(1), 10–22. https://doi.org/10.1002/(SICI)1099-0488(20000101)38:1<10::AID-POLB2>3.0.CO;2-6

Cheng, Y.-T., & Cheng, C.-M. (1998a). Scaling approach to conical indentation in elastic-plastic solids with work hardening. *Journal of Applied Physics*, *84*(3), 1284–1291. https://doi.org/10.1063/1.368196

Cheng, Y.-T., & Cheng, C.-M. (1998b). Relationships between hardness, elastic modulus, and the work of indentation. *Applied Physics Letters*, *73*(5), 614–616. https://doi.org/10.1063/1.121873

Cheng, Y.-T., & Cheng, C.-M. (1999). Can stress–strain relationships be obtained from indentation curves using conical and pyramidal indenters? *Journal of Materials Research*, *14*(9), 3493–3496. https://doi.org/10.1557/JMR.1999.0472

Cheng, Y.-T., & Cheng, C.-M. (2004). Scaling, dimensional analysis, and indentation measurements. *Materials Science and Engineering: R: Reports*, *44*(4–5), 91–149. https://doi.org/10.1016/j.mser.2004.05.001

Chollacoop, N., Dao, M., & Suresh, S. (2003). Depth-sensing instrumented indentation with dual sharp indenters. *Acta Materialia*, *51*(13), 3713–3729. https://doi.org/10.1016/S1359-6454(03)00186-1

Daphalapurkar, N. P., Dai, C., Gan, R. Z., & Lu, H. (2009). Characterization of the linearly viscoelastic behavior of human tympanic membrane by nanoindentation. *Journal of the Mechanical Behavior of Biomedical Materials*, *2*(1), 82–92. https://doi.org/10.1016/j.jmbbm.2008.05.008

DiCarlo, A., Yang, H. T. Y., & Chandrasekar, S. (2003). Semi-inverse method for predicting stress–strain relationship from cone indentations. *Journal of Materials Research*, *18*(9), 2068–2078. Cambridge Core. https://doi.org/10.1557/JMR.2003.0291

Field, J. S., & Swain, M. V. (1993). A simple predictive model for spherical indentation. *Journal of Materials Research*, *8*(2), 297–306. https://doi.org/10.1557/JMR.1993.0297

Futakawa, M., Wakui, T., Tanabe, Y., & Ioka, I. (2001). Identification of the constitutive equation by the indentation technique using plural indenters with different apex angles. *Journal of Materials Research*, *16*(8), 2283–2292. Cambridge Core. https://doi.org/10.1557/JMR.2001.0314

Gao, H., Cheng-Hsin, C., & Jin, L. (1992). Elastic contact versus indentation modeling of multi-layered materials. *International Journal of Solids and Structures*, *29*(20), 2471–2492. https://doi.org/10.1016/0020-7683(92)90004-D

Hadamard, J. (1902). Sur les problemes aux derivees partielles et leur signification physique. *Princeton University Bulletin*, 49–52. https://ci.nii.ac.jp/naid/10030001312/en/

Hadamard, J. (1932). *Le problème de Cauchy et les équations aux dérivées partielles linéaires hyperboliques*. Hermann et cie; /z-wcorg/.

Hall, J. J. (1967). Electronic Effects in the Elastic Constants of n -Type Silicon. *Physical Review*, *161*(3), 756–761. https://doi.org/10.1103/PhysRev.161.756

Harding, J. W., & Sneddon, I. N. (1945). The elastic stresses produced by the indentation of the plane surface of a semi-infinite elastic solid by a rigid punch. *Mathematical Proceedings* *of the Cambridge Philosophical Society*, *41*(1), 16–26. https://doi.org/10.1017/S0305004100022325

Heinrich, C., Waas, A. M., & Wineman, A. S. (2009). Determination of material properties using nanoindentation and multiple indenter tips. *International Journal of Solids and Structures*, *46*(2), 364–376. https://doi.org/10.1016/j.ijsolstr.2008.08.042

Hill, R. (1952). The Elastic Behaviour of a Crystalline Aggregate. *Proceedings of the Physical Society. Section A*, *65*(5), 349–354. https://doi.org/10.1088/0370-1298/65/5/307

Huang, G., Daphalapurkar, N. P., Gan, R. Z., & Lu, H. (2008). A Method for Measuring Linearly Viscoelastic Properties of Human Tympanic Membrane Using Nanoindentation. *Journal of Biomechanical Engineering*, *130*(1), 014501. https://doi.org/10.1115/1.2838034

Kavanagh, K. T. (1972). Extension of classical experimental techniques for characterizing composite-material behavior: The experimental-analytical method described in this paper is shown to yield material descriptions from specimen shapes previously considered intractable. *Experimental Mechanics*, *12*(1), 50–56. https://doi.org/10.1007/BF02320791

Kavanagh, K. T., & Clough, R. W. (1971). Finite element applications in the characterization of elastic solids. *International Journal of Solids and Structures*, *7*(1), 11–23. https://doi.org/10.1016/0020-7683(71)90015-1

Keryvin, V., Charleux, L., Bernard, C., & Nivard, M. (2017). The Influence of Indenter Tip Imperfection and Deformability on Analysing Instrumented Indentation Tests at Shallow Depths of Penetration on Stiff and Hard Materials. *Experimental Mechanics*, *57*(7), 1107–1113. https://doi.org/10.1007/s11340-017-0267-1

Lan, H., & Venkatesh, T. A. (2007). Determination of the elastic and plastic properties of materials through instrumented indentation with reduced sensitivity. *Acta Materialia*, *55*(6), 2025–2041. https://doi.org/10.1016/j.actamat.2006.11.012

Le Bourhis, E. (2008). Indentation mechanics and its application to thin film characterization. *Vacuum*, *82*(12), 1353–1359. https://doi.org/10.1016/j.vacuum.2008.03.077

Le, M.-Q. (2008). A computational study on the instrumented sharp indentations with dual indenters. *International Journal of Solids and Structures*, *45*(10), 2818–2835. https://doi.org/10.1016/j.ijsolstr.2007.12.022

Le, M.-Q. (2009). Material characterization by dual sharp indenters. *International Journal of Solids and Structures*, *46*(16), 2988–2998. https://doi.org/10.1016/j.ijsolstr.2009.03.027

Levenberg, K. (1944). A method for the solution of certain non-linear problems in least squares. *Quarterly of Applied Mathematics*, *2*(2), 164–168. https://doi.org/10.1090/qam/10666

Lichinchi, M., Lenardi, C., Haupt, J., & Vitali, R. (1998). Simulation of Berkovich nanoindentation experiments on thin films using finite element method. *Thin Solid Films*, *312*(1–2), 240–248. https://doi.org/10.1016/S0040-6090(97)00739-6

Lu, C.-J., & Bogy, D. B. (1995). The effect of tip radius on nano-indentation hardness tests. *International Journal of Solids and Structures*, *32*(12), 1759–1770. https://doi.org/10.1016/0020-7683(94)00194-2

Luo, J., & Lin, J. (2007). A study on the determination of plastic properties of metals by instrumented indentation using two sharp indenters. *International Journal of Solids and Structures*, *44*(18), 5803–5817. https://doi.org/10.1016/j.ijsolstr.2007.01.029

Ma, Z. S., Zhou, Y. C., Long, S. G., Zhong, X. L., & Lu, C. (2012). Characterization of stress-strain relationships of elastoplastic materials: An improved method with conical and pyramidal indenters. *Mechanics of Materials*, *54*, 113–123. https://doi.org/10.1016/j.mechmat.2012.07.006

Marquardt, D. W. (1963). An Algorithm for Least-Squares Estimation of Nonlinear Parameters. *Journal of the Society for Industrial and Applied Mathematics*, *11*(2), 431–441. https://doi.org/10.1137/0111030

Oliver, W. C., & Pharr, G. M. (1992). An improved technique for determining hardness and elastic modulus using load and displacement sensing indentation experiments. *Journal of Materials Research*, *7*(6), 1564–1583. https://doi.org/10.1557/JMR.1992.1564

Oliver, W. C., & Pharr, G. M. (2004). Measurement of hardness and elastic modulus by instrumented indentation: Advances in understanding and refinements to methodology. *Journal of Materials Research*, *19*(1), 3–20. Cambridge Core. https://doi.org/10.1557/jmr.2004.19.1.3

Pac, M.-J., Giljean, S., Rousselot, C., Richard, F., & Delobelle, P. (2014). Microstructural and elasto-plastic material parameters identification by inverse finite elements method of Ti (1−x) Al x N (0 < x < 1) sputtered thin films from Berkovich nano-indentation experiments. *Thin Solid Films*, *569*, 81–92. https://doi.org/10.1016/j.tsf.2014.07.037

Pelletier, H., Krier, J., & Mille, P. (2006). Characterization of mechanical properties of thin films using nanoindentation test. *Mechanics of Materials*, *38*(12), 1182–1198. https://doi.org/10.1016/j.mechmat.2006.02.011

Peng, G., Feng, Y., Huan, Y., & Zhang, T. (2013). Characterization of the viscoelastic-plastic properties of UPVC by instrumented sharp indentation. *Polymer Testing*, *32*(8), 1358–1367. https://doi.org/10.1016/j.polymertesting.2013.08.016

Phadikar, J. K., Bogetti, T. A., & Karlsson, A. M. (2013). On the uniqueness and sensitivity of indentation testing of isotropic materials. *International Journal of Solids and Structures*, *50*(20), 3242–3253. https://doi.org/10.1016/j.ijsolstr.2013.05.028

Pharr, G. M., Strader, J. H., & Oliver, W. C. (2009). Critical issues in making small-depth mechanical property measurements by nanoindentation with continuous stiffness measurement. *Journal of Materials Research*, *24*(3), 653–666. https://doi.org/10.1557/jmr.2009.0096

Qasmi, M., Delobelle, P., Richard, F., & Bosseboeuf, A. (2006). Effect of the residual stress on the determination through nanoindentation technique of the Young's modulus of W thin film deposit on SiO2/Si substrate. *Surface and Coatings Technology*, *200*(14), 4185–4194. https://doi.org/10.1016/j.surfcoat.2004.12.020

Qasmi, M., Delobelle, P., Richard, F., Brun, C., & Fromm, M. (2004). Viscoelastic mechanical properties determined by nanoindentation tests and its numerical modelling of polypropylene modified by He+ particle implantation and e− irradiation. *Progress in Organic Coatings*, *51*(3), 195–204. https://doi.org/10.1016/j.porgcoat.2004.07.012

Renner, E. (2016). *Vers l'identification d'une loi de plasticité monocristalline par analyse topographique d'empreintes de nanoindentation Berkovich* (Issue 2016BESA2059) [Thèse, Université de Franche-Comté]. https://tel.archives-ouvertes.fr/tel-01652133

Renner, E., Bourceret, A., Gaillard, Y., Amiot, F., Delobelle, P., & Richard, F. (2020). Identifiability of single crystal plasticity parameters from residual topographies in Berkovich nanoindentation on FCC nickel. *Journal of the Mechanics and Physics of Solids*, *138*, 103916. https://doi.org/10.1016/j.jmps.2020.103916

Richard, F. (1999). *Identification du comportement et évaluation de la fiabilité des composites stratifiés* [Thèse, Université de Franche-Comté]. /z-wcorg/.

Richard, F. (2017). *Vers une détermination guidée par l'identifiabilité du comportement mécanique des matériaux par nanoindentation* [Habilitation à diriger des recherches, COMUE Université Bourgogne Franche-Comté]. https://hal.archives-ouvertes.fr/tel-01590429

Richard, F., Villars, M., & Thibaud, S. (2013). Viscoelastic modeling and quantitative experimental characterization of normal and osteoarthritic human articular cartilage using indentation. *Journal of the Mechanical Behavior of Biomedical Materials*, *24*, 41–52. https://doi.org/10.1016/j.jmbbm.2013.04.012

Shih, C. W., Yang, M., & Li, J. C. M. (1991). Effect of tip radius on nanoindentation. *Journal of Materials Research*, *6*(12), 2623–2628. https://doi.org/10.1557/JMR.1991.2623

Sneddon, I. N. (1948). Boussinesq's problem for a rigid cone. *Mathematical Proceedings of the Cambridge Philosophical Society*, *44*(4), 492–507. https://doi.org/10.1017/S0305004100024518

Sneddon, I. N. (1965). The relation between load and penetration in the axisymmetric boussinesq problem for a punch of arbitrary profile. *International Journal of Engineering Science*, *3*(1), 47–57. https://doi.org/10.1016/0020-7225(65)90019-4

Swaddiwudhipong, S., Tho, K. K., Liu, Z. S., & Zeng, K. (2005). Material characterization based on dual indenters. *International Journal of Solids and Structures*, *42*(1), 69–83. https://doi.org/10.1016/j.ijsolstr.2004.07.027

Tho, K. K., Swaddiwudhipong, S., Liu, Z. S., Zeng, K., & Hua, J. (2004). Uniqueness of reverse analysis from conical indentation tests. *Journal of Materials Research*, *19*(8), 2498–2502. https://doi.org/10.1557/JMR.2004.0306

Torres-Torres, D., Muñoz-Saldaña, J., Gutierrez-Ladron-de Guevara, L. A., Hurtado-Macías, A., & Swain, M. V. (2010). Geometry and bluntness tip effects on elastic–plastic behaviour during nanoindentation of fused silica: Experimental and FE simulation. *Modelling and Simulation in Materials Science and Engineering*, *18*(7), 075006. https://doi.org/10.1088/0965-0393/18/7/075006

Tripp, M. K., Stampfer, C., Miller, D. C., Helbling, T., Herrmann, C. F., Hierold, C., Gall, K., George, S. M., & Bright, V. M. (2006). The mechanical properties of atomic layer deposited alumina for use in micro- and nano-electromechanical systems. *Sensors and Actuators A: Physical*, *130–131*, 419–429. https://doi.org/10.1016/j.sna.2006.01.029

Walter, E., & Pronzato, L. (1997). *Identification of parametric models from experimental data*. Springer ; Masson; /z-wcorg/.

Wang, L., Ganor, M., & Rokhlin, S. I. (2005). Inverse scaling functions in nanoindentation with sharp indenters: Determination of material properties. *Journal of Materials Research*, *20*(4), 987–1001. Cambridge Core. https://doi.org/10.1557/JMR.2005.0124

Wang, S., Liu, H., Xu, L., Du, X., Zhao, D., Zhu, B., Yu, M., & Zhao, H. (2017). Investigations of Phase Transformation in Monocrystalline Silicon at Low Temperatures via Nanoindentation. *Scientific Reports*, *7*(1), 8682. https://doi.org/10.1038/s41598-017-09411-x

Wang, T. H., Fang, T.-H., & Lin, Y.-C. (2007). A numerical study of factors affecting the characterization of nanoindentation on silicon. *Materials Science and Engineering: A*, *447*(1–2), 244–253. https://doi.org/10.1016/j.msea.2006.10.077

Yagawa, G., & Okuda, H. (1996). Neural networks in computational mechanics. *Archives of Computational Methods in Engineering*, *3*(4), 435. https://doi.org/10.1007/BF02818935

Yan, J., Karlsson, A. M., & Chen, X. (2007). Determining plastic properties of a material with residual stress by using conical indentation. *International Journal of Solids and Structures*, *44*(11), 3720–3737. https://doi.org/10.1016/j.ijsolstr.2006.10.017

Youn, S. W., & Kang, C. G. (2005). FEA study on nanodeformation behaviors of amorphous silicon and borosilicate considering tip geometry for pit array fabrication. *Materials Science and Engineering: A*, *390*(1–2), 233–239. https://doi.org/10.1016/j.msea.2004.08.041

Zhang, L., & Mahdi, M. (1996). The plastic behaviour of silicon subjected to micro-indentation. *Journal of Materials Science*, *31*(21), 5671–5676. https://doi.org/10.1007/BF01160813

Zhang, Y., Dhaigude, M., & Wang, J. (2015). The Anvil Effect in the Spherical Indentation Testing on Sheet Metals. *Procedia Manufacturing*, *1*, 828–839. https://doi.org/10.1016/j.promfg.2015.09.072

Zhao, M., Chen, X., Ogasawara, N., Razvan, A. C., Chiba, N., Lee, D., & Gan, Y. X. (2006). New sharp indentation method of measuring the elastic–plastic properties of compliant and soft materials using the substrate effect. *Journal of Materials Research*, *21*(12), 3134–3151. https://doi.org/10.1557/jmr.2006.0384

Zhao, M., Chen, X., Xiang, Y., Vlassak, J. J., Lee, D., Ogasawara, N., Chiba, N., & Gan, Y. X. (2007). Measuring elastoplastic properties of thin films on an elastic substrate using sharp indentation. *Acta Materialia*, *55*(18), 6260–6274. https://doi.org/10.1016/j.actamat.2007.07.045